

Duality of Wave Modulation and Nanotwinning in Ni-Mn-Ga Martensite via Long-Period Commensurate States

P. Veřtát¹ <vertat@fzu.cz> [ORCID: 0000-0002-0569-6436],
M. Zelený² <zeleny@fme.vutbr.cz> [ORCID: 0000-0001-6715-4088],
A. Sozinov³ <asozinov.fin@gmail.com>, [ORCID: N/A]
M. Klicpera⁴ <milan.klicpera@matfyz.cuni.cz> [ORCID: 0000-0002-3804-1268],
O. Fabelo⁵ <fabelo@ill.fr> [ORCID: 0000-0001-6452-8830],
R. Chulist⁶ <rchulist@agh.edu.pl> [ORCID: 0000-0001-6680-9636],
M. Vinogradova³ <Mariia.Vinogradova@lut.fi> [ORCID: 0000-0002-0917-5304],
P. Sedlák⁷ <psedlak@it.cas.cz> [ORCID: 0000-0002-0700-902X],
H. Seiner⁷ <hseiner@it.cas.cz> [ORCID: 0000-0002-1151-7270],
O. Heczko¹ <heczko@fzu.cz> [ORCID: 0000-0002-7647-3141],
and L. Straka¹ [**corresponding author**] <ladislav.straka@fzu.cz> [ORCID:0000-0003-1136-4996]
[Phone: +420 266 052 992]

¹ FZU – Institute of Physics of the Czech Academy of Sciences, Prague, Czechia

² Institute of Materials Science and Engineering, Faculty of Mechanical Engineering, Brno University of Technology, Brno, Czechia

³ Material Physics Laboratory, Lappeenranta-Lahti University of Technology LUT, Lappeenranta, Finland

⁴ Department of Condensed Matter Physics, Faculty of Mathematics and Physics, Charles University, Prague, Czechia

⁵ Institut Laue-Langevin, Grenoble, France

⁶ Faculty of Metals Engineering and Industrial Computer Science, AGH University of Science and Technology, Krakow, Poland

⁷ Institute of Thermomechanics of the Czech Academy of Sciences, Prague, Czechia

Data availability statement: The neutron diffraction data are available from Refs.^[62,63] Other data supporting this study's findings are available from the corresponding author upon reasonable request.

Conflict of interest: The authors declare no conflict of interest.

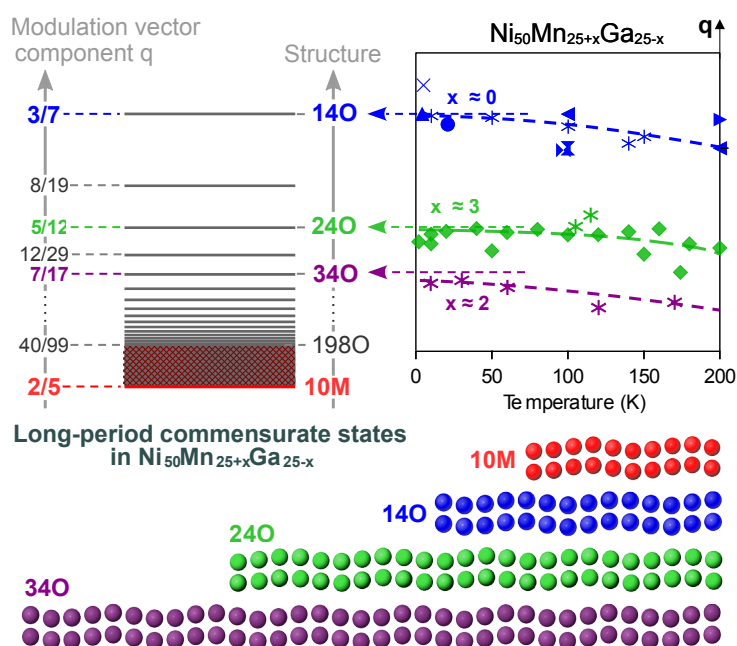
Funding statement: The authors acknowledge the Institut Laue-Langevin (ILL) for the beam time allocated, the funding support from the Czech Science Foundation [grant number 24-10334], Brno University of Technology [project number FSI-S-20-6313], and the assistance provided by the Ferroic Multifunctionalities project, supported by the Ministry of Education, Youth, and Sports of the Czech Republic [Project No. CZ.02.01.01/00/22_008/0004591], co-funded by the European Union. Computational resources were provided by the Ministry of Education, Youth and Sports of the Czech Republic under the Projects e-INFRA CZ (ID:90140) at the IT4Innovations National Supercomputing Center. We thank L. Klimša for assistance with scanning electron microscopy measurements.

ABSTRACT

Understanding the crystal structure of magnetic shape memory alloys is crucial for elucidating their martensite twin boundary supermobility and related functionalities. This study analyzes and discusses the structure of martensitic single crystals of $\text{Ni}_{50.0}\text{Mn}_{27.7}\text{Ga}_{22.3}$ and $\text{Ni}_{50.0}\text{Mn}_{28.1}\text{Ga}_{21.9}$. Neutron and X-ray diffraction reveal an anharmonic, incommensurate five-layer modulation that evolves with temperature. This evolution gives rise to two key microstructural features: i) periodic nanodomains, identified as emerging a/b -nanotwins, and ii) long-period commensurate structures, such as the 34O, 24O, and 14O states, whose orthorhombic unit cells inherently realize a/b -nanotwins. Ab initio calculations show that these long-period structures are energetically favorable, leading to a lock-in transition. In the alloys studied, the 24O state is the locked-in phase at low temperatures, whereas literature data indicate that $\text{Ni}_{50}\text{Mn}_{25}\text{Ga}_{25}$ (exact Ni_2MnGa stoichiometry) evolves toward the 14O phase. Crucially, these results unify two seemingly contrasting structural descriptions—wave-like modulation and discrete nanotwinning—thereby establishing a foundation for a deeper understanding of the crystal-structure-functionality relationship in magnetic shape memory alloys.

KEYWORDS: magnetic shape memory; structural modulation; long-period structure; nanotwinning; neutron diffraction

GRAPHICAL ABSTRACT



1 Introduction

The modulated crystal structures observed in Ni–Mn–Ga alloys exhibiting magnetic shape memory behavior are fundamental to their distinct properties, particularly their high twin boundary mobility.^[1-6] This mobility enables functionalities such as the magnetic field-induced strain of up to 12% and related magnetoelastic effects,^[7-9] thereby paving the way for emerging applications in actuation, sensing, and energy harvesting^[5].

Supermobility refers to exceptionally high twin boundary mobility across a broad temperature range.^[5,6] This property facilitates the development of energy-efficient devices functioning under diverse environmental conditions. It originates from an enormous shear elastic instability in the lattice, with an elastic anisotropy ratio (A^*)^[10] reaching up to 255. This exceptionally soft shearing is attributed to stress-induced discrete defects within the structural modulation (changes in the modulation stacking sequence).^[6] Numerous studies also suggest an interplay between the modulation and high mobility/supermobility,^[11-13] emphasizing the need for a detailed analysis of the structural modulation.

The five-layer modulated martensite is the most extensively studied modulated structure in Ni–Mn–Ga. It is termed 10M when chemical ordering is considered and 5M when it is not. Despite extensive research, the modulation of this martensite has not yet been comprehensively understood. The modulation appears as a continuous wave in diffraction experiments^[14,15] but is observed as an assembly of nanotwinned blocks in high-resolution atomic imaging,^[13,16] which initially seems contradictory. Moreover, while variations in crystal structure and modulation have been reported, their origins remain unexplained.

Three primary structural cases of five-layered martensite have been identified based on powder diffraction^[14,17,18] and high-resolution single-crystal diffraction studies:^[19]

- i) A *monoclinic* commensurate (C) modulated structure with $q \approx 2/5$ (observed in $\text{Ni}_{50}\text{Mn}_{28}\text{Ga}_{22}$ at room temperature),
- ii) An *orthorhombic* incommensurate (IC) modulated structure with $q \approx 3/7$ (in $\text{Ni}_{50}\text{Mn}_{25}\text{Ga}_{25}$ at low temperatures), and
- iii) A *monoclinic* or *orthorhombic* IC modulated structure with $2/5 < q < 3/7$ (with q dependent on temperature).

In every case, the symbol q represents the modulation vector component—a scalar related to the modulation periodicity. In cubic ($L2_1$ -frame) coordinates (a , b , c ; see inset in **Figure 1c**), the modulation vector is expressed as $\mathbf{q} = q \cdot \mathbf{g}_{110}^* = (q, q, 0)^*$, where \mathbf{g}_{110}^* is the $(1, 1, 0)^*$ reciprocal space vector. Using the smallest possible face-centered tetragonal unit cell (often denoted as $L1_0$ ^[20])—or “*diagonal coordinates*” (a_d , b_d , c_d ; see inset in **Figure 1c**)—the modulation vector is expressed as $\mathbf{q}_d = q \cdot \mathbf{g}_{001d}^* = (0, 0, q)_d^*$.^[17] No published study reports any deviation of the modulation vector from this direction. Hence, characterizing the modulation solely by the component q is universal for both coordinate systems.

The crystal structure and modulation vector component q vary with composition (cases i and ii) and temperature (case iii). However, temperature-dependent studies^[15,17,18,21] have not explored the underlying mechanisms of structural evolution. A key question remains: What drives the thermal evolution of the modulation, and how does this evolution manifest in the crystal structure and microstructure?

The uncertainties regarding the modulation character (wave versus nanotwinned, commensurate versus incommensurate) and the crystal symmetry (monoclinic versus orthorhombic)—crucial for understanding supermobile twin boundaries—strongly motivated the detailed experimental and theoretical investigations presented here. We build upon our recent findings from single-crystal neutron diffraction conducted with high resolution along the modulation direction.^[22] These findings reveal that the seemingly different crystal structures are simply variations of the same anharmonic modulation function, differing primarily in period and amplitude. Thus, rather than interpreting observations reported by various authors as crystal structures with distinct symmetries, they can be understood as manifestations of a single, evolving universal structure. This broader perspective, which aids in formulating and understanding the physical mechanisms governing lattice distortions, is further explored in this study.

Earlier works^[23,14,24] considered the modulation function as a sum of harmonic functions but limited their expansion to the third harmonic. This approach cannot capture all the features of the diffraction patterns obtained. The anharmonic modulation function that includes contributions from higher harmonics (fifth and eighth) is therefore more appropriate:^[22]

$$dx = A_1 \cdot \sin(2\pi z/p) + 0.2 \cdot A_1 \cdot \sin(5 \cdot 2\pi z/p) + 0.04 \cdot A_1 \cdot \sin(8 \cdot 2\pi z/p), \quad (1)$$

where dx is the displacement of the whole (110) plane along the $[1\bar{1}0]$ direction in cubic coordinates $((001)_D$ and $[100]_D$ in diagonal coordinates, Figure 1c), A_1 represents the amplitude of the fundamental harmonic, z denotes the coordinate along the modulation direction (lattice plane number $z = 0, 1, 2, \dots$), and

$$p = 2/q \quad (2)$$

is the modulation period measured in lattice planes.

A commensurate modulation means that the modulation period is in a rational ratio with the lattice periodicity; in other words, the modulation vector component q (as well as $p = 2/q$) is a rational number. When multiple modulation periods must combine to achieve alignment with the lattice, the structure is referred to as *long-period commensurate* (LP-C). To our knowledge, long-period commensurate structures (or states) have not yet been systematically explored in Ni-Mn-Ga. As q evolves between 0.400 and 0.428, many LP-C states inevitably emerge since every non-empty continuous interval of real numbers contains infinitely many rational numbers.

A series of commensurate-incommensurate-commensurate transitions are well-documented experimentally in many materials with long periodicity along a unique direction.^[25,26] LP-C states, often energetically favorable, can appear over certain temperature intervals. In the $q(T)$ dependence, this manifests as staircase-like steps, a phenomenon commonly referred to as the *devil's staircase*.^[27,28] With decreasing temperature, the structure can lock into a specific low-energy LP-C state, a process known as the *lock-in* transition. Consequently, LP-C structures are found as the ground states in many systems. The typical progression of the lock-in transition includes: i) a high-symmetry phase transforming into an incommensurately modulated structure, ii) the formation of commensurate regions separated by discommensuration regions on the microscale as temperature decreases, and iii) a final lock-in into an LP-C modulated phase. However, in many materials, the link between the microscopic rearrangement and the IC→LP-C lock-in transition is yet to be elucidated.

In this report, we present the results of our recent collaborative effort aimed at comprehensively describing the effect of temperature-induced evolution of structural modulation on the microstructure of the prototype magnetic shape memory alloy. We first describe the anharmonic nature of the structural modulation in Ni–Mn–Ga, focusing on two exceptional compositions that retain a five-layer modulation at low temperatures. Building on this finding, we show how the evolving lattice incommensurability leads to the formation of nanodomains, changes in lattice symmetry, and the emergence of long-period commensurate states. An *ab initio* (DFT+U) analysis further explains why long-period states outcompete the shortest-period structure. In addition, we incorporate literature data to identify distinct long-period commensurate structures in commonly studied compositions. Finally, we envision how these findings—combined with the concept of phasons—might yield better control over the elastic and functional properties of Ni–Mn–Ga alloys.

2 Results and Discussion

2.1 Anharmonic incommensurate modulation

This Section reviews our neutron and X-ray diffraction experiments on single crystals and validates the anharmonic modulation model against the data. We also show that the continuous modulation wave can be regarded as a stacking sequence of basal planes, which later aids in describing modulation-induced microstructural features.

Figure 1a presents a schematic phase diagram of the $\text{Ni}_{50}\text{Mn}_{25+x}\text{Ga}_{25-x}$ (at. %) system.^[29] The measurement paths for the studied compositions are marked, clarifying each alloy's compositional position and projected phase evolution. The selected compositions $x = 2.7$ ($\text{Ni}_{50.0}\text{Mn}_{27.7}\text{Ga}_{22.3}$, alloy 1) and $x = 3.1$ ($\text{Ni}_{50.0}\text{Mn}_{28.1}\text{Ga}_{21.9}$, alloy 2) show no intermartensite transformations, allowing a focused investigation of the five-layered martensite down to 2 K.

Figure 1b shows examples of neutron diffraction (ND) q -scans for alloy 2 at various temperatures. The figure also illustrates the link between the modulation vector component q and the spacing of satellite reflections. Figures 1c and 1d present the temperature-dependent evolution of q in alloys 1 and 2, respectively, determined from average satellite spacing. Both alloys are nearly

commensurate (C) at room temperature near the martensite transformation, with $q \approx 2/5$, which converges to $q \approx 0.416$ at low temperatures. In our previous report, we fitted the entire calculated diffraction pattern to the experimental data rather than determining q solely from satellite spacing.^[22] Both methods yield similar $q(T)$ dependences with a precision of approximately ± 0.001 .

Figure 1b additionally highlights high-order diffraction satellites in the incommensurate (IC) structure. This rich satellite landscape, also seen for X-ray diffraction (XRD, **Figure 2**), stems from the interplay between incommensurability and anharmonicity in the modulation function and effectively reveals its spectral content.^[22] It is customary to include harmonics of the modulation function up to the order of the highest distinct satellite reflection observed.^[30,31] In the modulation function according to Equation (1), there is a substantial 20% contribution to the displacement amplitude from the fifth harmonic, reflecting the prominent fifth-order satellites in experimental diffraction patterns (peaks closest to the main reflections, as shown in Figure 2d). Even though the eighth harmonic term is much weaker, its inclusion is justified by the non-negligible intensity of the eighth-order diffraction satellite, as indicated in Figure 2d (see Ref.^[22] for further supporting data), and it also significantly improves the fits of the experimental diffraction patterns.

Detecting satellites up to the eighth order far exceeds typical experimental observations, where even third-order satellites are rare, and measurable intensity from satellites beyond the fourth order is exceptionally uncommon.^[31,32] Singh et al.^[33] noted that a conventional laboratory-source powder XRD setup cannot detect the second and third-order satellites of the martensite phase of Ni_2MnGa . Moreover, including higher-order harmonics in the refinement process leads to highly correlated parameters, which can cause the refinement to fail.^[31] Consequently, conventional methods may not reveal the strongly anharmonic character of the modulation. Therefore, high-resolution and high-intensity techniques—such as synchrotron-based or single-crystal diffraction—are essential for accurate determination of the modulation function.

The evaluation of neutron diffraction patterns for the single crystal of alloy 1 and their comparison with model calculations have been presented in previous work.^[22] Hence, we do not repeat that analysis here; instead, Figure 2 compares selected experimental X-ray diffraction (XRD) patterns for single crystals of alloy 2 with model-calculated diffraction patterns. The model parameters were q and A_1 . In fact, A_1 can be expressed as a function of q , effectively reducing the free parameters in the model to just q . The diffraction patterns calculated using the modulation function from Equation (1) closely match the experimental data in Figure 2. Similarly strong fits were obtained for both XRD and ND at all measured temperatures for both alloys.

Some variations in the modulation function amplitude (A_1) were observed among different alloys and experiments. They are attributed to various experimental factors such as sample history, composition, and modulation twinning (see *Experimental Section* and Ref.^[2] for the respective explanation of twinning systems). When modulation twins are present, the diffraction satellites spread along multiple directions rather than just one, reducing their overall intensity. This can affect the determined modulation amplitude.^[22]

Nevertheless, the overall picture remained consistent in our experiments: the modulation function contained significant higher-harmonic components, particularly the fifth and eighth harmonics, and its amplitude A_1 increased as the temperature decreased. At room temperature, A_1 was approximately 5–7% (≈ 30 pm) of the d_{110} plane spacing, rising to approximately 8–10% (≈ 40 pm) of d_{110} at 10 K. Previous studies have reported comparable modulation amplitudes of 6–10%.^[14,24]

While modulation is typically described as a continuous displacement wave, an alternative, equally insightful approach is to interpret it as a stacking sequence of basal planes or other larger structural blocks.^[34,35] In **Figure 3**, this is illustrated for commensurate $q = 2/5$ modulation, demonstrating how modulation displacements can be interpreted as a $(2\bar{3})_2$ stacking sequence of (110) basal planes. The $(2\bar{3})_2$ denotes a sequence in which the $(2\bar{3})$ unit is repeated twice to align with chemical order; the notation is retained for consistency with prior studies, though chemical ordering is not essential here.

Figure 3a shows the displacements at the same scale as the lattice. Figure 3b exaggerates the displacements threefold to reveal better the similarity between the continuous modulation and the zig-zag-like stacking sequence. Figure 3c juxtaposes the modulation function with the lattice periodicity (vertical lines), demonstrating how the resulting basal plane displacements emerge from the interplay between the modulation function and the discrete lattice. These visualizations underscore that the stacking sequence arises naturally from continuous modulation rather than representing an independent structural feature.

Taken together, these findings robustly validate our structural model based on an anharmonic modulation function, which accurately captures the rich satellite landscape observed in the diffraction patterns. The excellent agreement between experimental neutron and X-ray diffraction data and model predictions—spanning a broad temperature range of approximately 300 K in two compositionally distinct alloys—underscores the reliability of our approach. Interpreting the modulation as a stacking sequence of basal planes helps to understand how the atomic arrangement adapts to changing modulation. This will be explored further in the next Section, where we analyze microstructural changes driven by modulation period growth.

2.2 Nanodomains and a/b -nanotwins

This Section examines how the thermal evolution of q drives the larger-scale structural—or microstructural—changes. First, we show that incommensurate anharmonic modulation drives nanodomain formation. Next, we interpret the modulation as a stacking sequence of basal (110) planes, revealing that these nanodomains are emerging a/b -nanotwins. Finally, we present experimental evidence and identify specific long-period commensurate states whose orthorhombic unit cells simultaneously manifest as a/b -nanotwins ($\{110\}$ compound; see Experimental Section for details on twinning systems).

2.2.1 Nanodomain formation

Nanodomains arise from the mismatch between the periodicity of the modulation and that of the lattice. **Figure 4** demonstrates the concept, beginning with a well-known phenomenon from acoustics in Figure 4a. When two signals of slightly different frequencies f_1 and f_2 are summed, the resulting signal exhibits “beats” or an “amplitude envelope”, i.e., periodic fluctuations in amplitude, with frequency $|f_1 - f_2|$. A similar phenomenon arises when a continuous wave interacts with a discrete series of pulses, also yielding an amplitude envelope with a lower frequency, as illustrated in Figure 4b. This situation parallels our structural study, where the modulation function (continuous) interacts with the lattice (discrete).

Figure 4c illustrates the effect for our specific case of five-layer modulation. We compare displacements for commensurate modulation ($q = 2/5 = 0.400$) and incommensurate modulation ($q = 0.412$). In the commensurate case, atomic displacements exhibit a perfectly repeating pattern every five lattice planes. In contrast, in the incommensurate case, the mismatch in periodicity causes atomic displacements to vary over longer distances, manifesting as the displacement envelope. Each envelope period can be ascribed to a structural domain with a well-defined microstructure, which will be described in the next Section.

A larger-scale depiction of the formed domains is given in Figure 4d, highlighting their size depending on q . The following equation determines the domain size (DS):

$$DS = \left(\frac{5}{5-p} - 1\right) \cdot d_{110} = \left(\frac{2}{5q-2}\right) \cdot d_{110} \quad (4 < p < 5, 2/5 < q \leq 1/2), \quad (3)$$

where the modulation period $p = 2/q$ is measured in lattice planes, and d_{110} represents the interplanar distance along the modulation direction [110]. The domain size is infinitely large in an ideal, exactly commensurate structure ($q = 2/5, p = 5$). However, even for a very small incommensurability, e.g., as that observed at room temperature, the domain size gets to the submicron scale ($DS \approx 1000$ nm for $p \approx 4.999$, i.e., $q \approx 0.4001$). As q increases, the modulation period p further decreases, resulting in even smaller domains. Hence, in most cases, the domains will be of a nanoscopic scale; therefore, they are called *nanodomains* hereafter.

Thus, we find that the incommensurate nature of the modulation gives rise to nanodomains whose size is controlled by the modulation period $p = 2/q$.

2.2.2 Emerging *a/b*-nanotwins

Next, we link the found nanodomains with discrete structural features, making it easier to understand what these nanodomains represent and how the modulation evolution is reflected in the structure and microstructure. This is achieved by interpreting modulation displacements as a basal (110) plane stacking sequence.

A straightforward example of commensurate modulation is detailed in Figures 3 and 4c, illustrating continuous modulation interpreted as a stacking sequence. A consistent pattern of two positive ("up") shifts and three negative ("down") shifts emerges, corresponding to the specific infinite $(2\bar{3})_2$ stacking sequence. Vinogradova et al.^[36] recently showed that the *average lattice* of the commensurate phase of Ni-Mn-Ga-Fe martensite can be accurately described using the stacking plane sequence with a *constant plane shift* (CPS model), in line with earlier similar concepts^[34,35].

However, the plane shifts must vary to accurately capture the determined anharmonic incommensurate modulation according to Equation (1), thereby exactly reproducing the modulation displacements. Qualitatively, each plane shift remains either positive (+1) or negative (-1), mostly maintaining the $(2\bar{3})_2$ -like sequence, as shown in Figure 3. In the incommensurate regime, however, local faults develop in the $(2\bar{3})_2$ sequence due to periodicity mismatches. As q increases and the modulation period shortens, a repeating pattern of $2\bar{2}$ -like faults emerges within the $(2\bar{3})_2$ sequence (Figures 4c and 4d), thereby modifying the original 10M structure. Further, the $2\bar{2}$ -like faults are marked as $2|\bar{2}$ interfaces, with "|" indicating the center of the interface or nanotwin boundary, as described next.

The stacking sequence perspective enables us to correlate the atomic-scale displacements with larger-scale structural features such as twin boundaries and nanodomains. The displacements in the incommensurate structure interpreted as a stacking sequence are given in Figure 4c. Periodic reversals occur between $(2\bar{3})_2$ and $(\bar{2}3)_2$ stackings, separated by $2|\bar{2}$ interfaces. Such reversals correspond to the structural model of a/b -nanotwins as inverting stacking faults.^[13,37,38] The "|" symbol then represents the nanotwinning plane, separating the two nanotwin domains. Furthermore, beyond its alignment with the inverting stacking sequence model of a/b -nanotwins, the $(2\bar{3})_2$ stacking induces a shear, mirrored in the opposite $(\bar{2}3)_2$ stacking. This is consistent with the continuum theory view of a compound twin as two oppositely sheared domains.

Therefore, the mismatch in periodicity inherently triggers the formation of a/b -nanotwins. Although the model is purely mechanistic, it aligns well with *ab initio* calculations of fault energies. The model does not predict $3|\bar{3}$ twin interfaces, which have been shown to exhibit high energy, whereas the predicted $2|\bar{2}$ interfaces were calculated as the most energetically favorable.^[29,38] These interfaces correspond to a $(2\bar{2})$ stacking sequence—that is, the 4O structure^[39], briefly discussed in Section 2.5.

The low energy associated with the $(2\bar{2})$ stacking sequence further supports the interpretation of the incommensurate sequence as an incipient a/b -nanotwin. Incommensurability initially produces a stacking sequence resembling a/b -nanotwinning. The system can then relax locally to minimize energy and transform the apparent nanotwin into a true a/b -nanotwin. In particular, all $2\bar{2}$ -like faults will presumably be driven into the same perfect symmetrical $2|\bar{2}$ twin boundary as seen in the well-defined 4O structure. Local relaxations may also occur within the $(2\bar{3})_2$ -like segments, adjusting them toward the configuration characteristic of the commensurate 10M structure (as shown in Figure 3; see Section 2.3 for further discussion on a/b -nanotwins in LP-C states).

Note that "*a/b-nanotwins*" differ from the "*adaptive nanotwins*" commonly observed in tetragonal systems^[40]. In the adaptive concept of Ni–Mn–Ga martensite^[13,41,42], the modulated structure is viewed as nanotwinned tetragonal $c/a > 1$ (non-modulated, NM) martensite, where *each* $2|\bar{3}$ or $\bar{2}|3$ interface represents a twin boundary. The adaptive tetragonal nanotwin spans *five lattice planes* and thus is the lowest-scale (micro)structural feature. In contrast, the *a/b-nanotwins* are formed at one scale level higher and can span from *ten to about a hundred lattice planes* (see also adaptive diffraction condition in the next Section and atomic arrangement in Section 2.3).

The proposed model and mechanism establish a theoretical framework for nanodomain and *a/b-nanotwin* formation. However, experimental validation remains essential. The following Section presents supporting evidence.

2.2.3 Experimental confirmation

Direct observation of *a/b-twin* refinement upon cooling can strongly support the evolving nanodomains and *a/b-nanotwinning* hypothesis.

The *a/b-twins* are difficult to observe because of their small twinning shear, resulting in minimal misorientation ($<0.2^\circ$) and an almost undetectable difference in the *a* and *b* lattice parameters ($a/b < 1.005$). Despite these challenges, several studies have directly imaged *a/b-twins* using scanning/transmission electron microscopy (SEM/TEM). The methods included direct TEM imaging^[13] and manually indexed electron backscattered diffraction (EBSD) in SEM.^[43] In backscattered electron (BSE) imaging in SEM^[44,45], electron channeling effects enhance visibility. Optical observations of broad twins have also been demonstrated.^[46]

Using BSE contrast in SEM, we observed the evolution of *a/b-twins* with cooling in the Ni_{50.0}Mn_{28.2}Ga_{21.8} alloy, as shown in **Figure 5**. At 298 K and $q \approx 0.400$, broad *a/b-twin* bands are discernible (Figure 5a). However, at 253 K and $q > 0.400$, significantly finer twin bands appear in the same region (Figure 5b). Thus, the same sample region imaged at two different temperatures reveals a dramatic refinement of *a/b-twins*. A broader set of observations shows a continuous refinement of *a/b-twins* upon cooling and a coarsening of *a/b-twins* upon heating, aligned with the hysteresis in the $q(T)$ dependency.^[29] We also found similar thermal refinement and broadening of twins—aligned with q deviating from and returning to ≈ 0.400 —in the five-layered martensite of Ni₅₀Mn₂₇Ga₂₂Fe₁.^[15]

Therefore, the formation of finer domains with increasing q is well-supported by our observations. However, the direct in situ correlation of local domain size and q is not feasible because SEM typically does not measure q . Instead, we estimate the average domain size using the *adaptive diffraction*^[47,48] condition, i.e., a condition relating to nanodomain size and diffraction peak merging. (Note: "*Adaptive diffraction*" is unrelated to "*adaptive martensite*" and refers solely to a specific diffraction condition.)

For nanoscopic twin domain size, the *adaptive diffraction* occurs under condition $m < 2/(sh)$, where m is twin width in atomic planes, s is the twinning shear, and h is the cubic reciprocal space coordinate of the measured (h00) reflection. The critical domain size is around 20 nm for a typical

Ni-Mn-Ga alloy.^[37] This 20 nm threshold marks the point at which the (400) and (040) reflections merge, signaling a symmetry shift from monoclinic to orthorhombic. Above this size, the (400) and (040) reflections corresponding to the a and b axes are separated; below ≈ 20 nm, they merge into a single (400)' reflection.

Thus, merging (400) and (040) reflections, or the corresponding lattice parameters, can serve for robust quantitative estimation of an average a/b -nanotwin size. For measured $a \neq b$, the a/b -nanotwins are larger than ≈ 20 nm, while for measured $a = b$, they are smaller than ≈ 20 nm. Simultaneously, these changes lead to an apparent shift between monoclinic and orthorhombic symmetry.^[37] The relation between a and b lattice parameters and symmetry is illustrated in the inset in **Figure 6a**.

Figure 6a shows the experimental lattice parameters a and b in alloy 1 as a function of temperature, alongside the corresponding nanodomain (a/b -nanotwin) size versus temperature. The latter relationship was derived from Equation (3) using the experimental $q(T)$ dependence (Figure 1c). The nanodomain size decreases with cooling. The 20 nm domain size is indicated, below which the adaptive diffraction condition is met.

The temperature at which the predicted domain size of 20 nm is reached (using experimental $q(T)$ in Equation (3)) aligns closely with the temperature where adaptive diffraction occurs (where a equals b upon cooling). Specifically, these temperatures were about 290 K and 295 K, respectively, which is a negligible difference when accounting for experimental uncertainties. In other words, adaptive diffraction (manifested experimentally as $a = b$) confirms the predicted domain size of ≈ 20 nm calculated from experimental $q(T)$ using Equation (3).

In summary, our BSE and XRD observations provide direct experimental evidence for nanodomains (a/b -nanotwins) forming below approximately 290 K. These observations of nanodomains and a/b -nanotwinning set the stage for the emergence of long-period commensurate states, which we discuss in the next Section.

2.3 Long-period commensurate states

As shown above, nanodomains develop within the evolving incommensurate structure and can be interpreted as emerging a/b -nanotwins. As this evolution progresses, long-period commensurate (LP-C) states arise with rational q . This occurs when an integer multiple (N) of the modulation period p aligns with the lattice periodicity, i.e., when $N \cdot p$ is an integer number of lattice planes. This commensurability condition— also illustrated in Figure 6b—can be expressed as:

$$p = 5 - 1/N, \text{ where } N = 1, 2, 3, \dots, \quad (4)$$

and the length of the long period (LP) is:

$$LP = N \cdot p = 5N - 1 \quad (5)$$

The determined long-period commensurate states are listed in **Table 1**, illustrating the relationship between N , the modulation period p , the modulation vector component q , and the corresponding domain size for each state. At one extreme, $N = 1$ yields the theoretically predicted 4O structure^[39] ($q = 1/2$), which has not been experimentally observed in Ni-Mn-Ga. At the other extreme, $N = \infty$ corresponds to $q = 2/5$, which represents the 10M commensurate structure.

For LP-C states, q and p are always rational fractions. These can be derived from $p = 2/q$ and Equation (4) as:

$$q = \frac{2N}{(5N-1)}, \quad p = \frac{5N-1}{N}, \quad (6a, 6b)$$

as also listed for q in Table 1.

The domain size of LP-C states is calculated from Equation (3) using the lattice spacing $d_{110} = 0.21$ nm. The structure naming convention in Table 1 follows Ramsdell notation—commonly used in polytype structures—based on the unit cell size and symmetry. For example, 24O represents an orthorhombic unit cell with 24 stacking planes. An alternative notation is also proposed based on the modulation period p and symmetry, which may be more practical in some cases. Under this scheme, 24O is denoted 4.800O.

The structures with $DS > 20$ nm (i.e., 99 lattice planes, $N > 20$, $q \geq 0.404$) are labeled M (monoclinic) in Table 1. This labeling reflects that the symmetry remains monoclinic until the adaptive diffraction condition is crossed, shifting to orthorhombic (Figure 6c). Consequently, three structural regimes are identified:

- i) Commensurate monoclinic structure for $q = 2/5$ (10M-C).
- ii) Incommensurate monoclinic structure for $2/5 < q < 0.404$ (10M-IC).
- iii) Orthorhombic structure for $0.404 \leq q \leq 3/7$ (IC and LP-C states - 14O, 24O, ...).

The long-period commensurate structures exhibit orthorhombic symmetry. The cases most relevant for this study—14O ($q = 3/7$), 24O ($q = 5/12$), and 34O ($q = 7/17$)—are marked in Figure 6c, and their unit cells are illustrated in **Figure 7**. The stacking sequence interpretations in the same figure show $2|\bar{2}$ nanotwin boundaries and inversions of the $(\bar{3}2)$ sequence to $(\bar{2}3)$ and vice versa. This reveals that, in addition to aligning with the lattice periodicity, the unit cells in long-period commensurate states also represent a perfect a/b -nanotwin.

Specifically, the determined sequences are: i) $(\bar{2}\bar{3}2|\bar{2}\bar{3}\bar{2})$ for 14O, ii) $(\bar{2}\bar{3}\bar{2}\bar{3}2|\bar{2}\bar{3}\bar{2}\bar{3}\bar{2})$ for 24O, and iii) $(\bar{2}\bar{3}\bar{2}\bar{3}\bar{2}\bar{3}2|\bar{2}\bar{3}\bar{2}\bar{3}\bar{2}\bar{3}\bar{2})$ for 34O, where "|" again represents the a/b -nanotwin boundary separating the "left" and "right" nanotwin domain.

Both studied alloys converge toward $q \approx 0.416$ ($5/12$) at low temperatures (Figure 1c, d). This value matches the 24O long-period commensurate state (Table 1), indicating that 24O is energetically favored over incommensurate states at low temperatures. This convergence signifies a lock-in transition, in which the modulation becomes fixed at a commensurate value, a phenomenon well-documented in materials exhibiting long periodicity.^[25,26]

Thus, we identify specific long-period commensurate (LP-C) states, manifesting orthorhombic unit cells that also realize a/b -nanotwins. As temperature decreases, the lock-in transition to the 24O state is confirmed experimentally in alloys 1 and 2.

2.4 a/b -nanotwins under stress

With an understanding of the structural landscape of a/b -nanotwins, notably their size and the occurrence of LP-C states, we can further characterize them in experiments. Here, we demonstrate only the initial probing of stress response; a broader study exceeds the scope of this report.

Following the previous reasoning on nanodomain size and Equation (3), we can link q to a/b -nanotwin size and vice versa. In an ideal, perfectly commensurate 10M structure with $q = 2/5$, which lacks inherent inversion of $(2\bar{3})_2$ stacking, the a/b -twins are of infinite size. In the experiment, a/b -twins of size $10^1 \mu\text{m}$ or smaller are observed^[43] (see also Figure 5). Such twin size corresponds to a minuscule deviation of q from $2/5$. Since sequence inversion in a/b twins is connected with an opposite shear (see also discussion on 10M and 10O in the next Section), the a/b -twins can be manipulated through usual twinning mechanisms, such as lattice compliance with stress.

Saren et al.^[46] observed stress-induced redistribution of a/b -twins in 10M martensite of $\text{Ni}_{50.0}\text{Mn}_{28.4}\text{Ga}_{21.6}$. The location in the phase diagram (Figure 1a) indicates that this alloy was in a commensurate or near-commensurate state at room temperature. The observed twin sizes ranged between 1 to 10 μm , which, using Equations (2) and (3), corresponds to $q < 0.40001$. These a/b -twins reoriented under very low applied stress ($\approx 0.1 \text{ MPa}$).

However, the stress required for twin reorientation increases, and lattice softness decreases when the structure approaches the 14M martensite.^[15,49] At that stage, $q \gg 0.4$, and the a/b -nanotwins refine to a size of a few tens of atomic planes. We examine how such an a/b -nanotwinned structure responds to in-situ tensile loading along $[100]$ in synchrotron (details forthcoming; see also Ref.^[50]). The tensile strain was determined from lattice spacing measurements, similar to the method in Ref.^[51]

The studied sample initially had $q = 0.414$, which is located between the 24O and 34O structures (Figure 6c) and corresponding to an $\approx 6 \text{ nm}$ a/b -twin size. Figure 6d illustrates how the structure evolved under increasing strain. Notably, q remained nearly constant until a strain of $\approx 0.15\%$, where a transition to a mixed IC-C state occurred. This state consisted solely of the initial $q = 0.414$ phase and the commensurate $q = 2/5$ phase. Further strain led to a fully commensurate state, eliminating unfavorable a/b -nanotwin orientations and producing large untwinned regions with a long a -axis along the stress^[51].

The specific evolution of q upon loading indicates that the a/b -nanotwins—although not locked in an LP-C state—are firmly anchored within the structure. They do not rearrange (change size) under loading until a critical point, at which they (locally) annihilate, instantly changing the structure to a fully commensurate state. This evolution suggests that continuous wave modulation, rather than discrete nanotwin rearrangement, is behind the formation and thermal evolution of the incommensurate structure. However, theoretical analysis indicates that a/b -nanotwinning still contributes to the low energy of the structure.^[38]

2.5 Energy landscape from *ab initio* calculations

Our diffraction experiments and accompanying analysis reveal the existence of the long-period commensurate state 24O, toward which the structure converges upon cooling. The central question is: What drives the system to favor long-period commensurate states at low temperatures, i.e., how does the energy evolve with changing q ? *Ab initio* calculations using the DFT+U method can address this question. However, given their limited predictive power^[52], these calculations must first be validated against the anharmonic modulation model and other experimental data, such as the 10M and 4O structure stability.

Figure 8 gives an overview of the DFT+U results. Figure 8a compares the modulation function from Equation (1) with the relative displacements in the 24O structure determined by DFT+U. Except for a slight amplitude difference—dependent on the localization correction parameter U —the displacement profiles are nearly identical. This indicates good agreement between the *ab initio* calculation and our anharmonic modulation model. In contrast, a comparison with a purely harmonic wave in the same plot reveals significant discrepancies. This confirms that describing the modulation as purely harmonic or near-harmonic is insufficient, consistent with earlier *ab initio* calculations. In particular, Gruner et al.^[38] demonstrated that harmonic modulation is applicable only for small modulation amplitudes. These can be linked to the onset of martensite transformation when the harmonic soft-phonon mode of austenite plays a significant role. The modulation is anharmonic for large amplitudes, reflecting nanotwinning within the formed martensite.

Figure 8b shows that increasing the localization correction parameter U results in a systematic decrease in the modulation amplitude. We define amplitude Δ as half the difference between the calculated cell's maximum positive and minimum negative displacement. It relates to the experimental modulation amplitude A_1 (Equation (1)) as $\Delta \approx 1.24 \cdot A_1$. For $U = 0$, $\Delta = 11.5\%$ of d_{110} , and decreases about linearly with U to $\Delta = 8.2\%$ of d_{110} for $U = 1.8$ eV. This range of Δ corresponds reasonably to that observed experimentally, $1.24 \cdot A_1 = 12.4\%$ for alloy 1 at 10 K and $1.24 \cdot A_1 = 9.4\%$ for alloy 2 at 2 K. The reasons for experimental amplitude variation are discussed in Section 2.1.

To summarize the initial validation, for the considered range of U , both the modulation waveform from DFT+U calculations (Figure 8a) and its amplitude (Figure 8b) agree well with the experimental data and the anharmonic modulation model using Equation (1).

The energy landscape—i.e., a plot of energies for individual commensurate structures with different q values under various Hubbard corrections U —is shown in Figure 8c. To minimize errors due to cell-size effects, the energies are given relative to the energy of non-modulated martensite with the same calculation cell size. The 4O ($p = 4$) and commensurate 10M ($p = 5$) structures have been studied before (e.g., Refs.^[38,39]). In contrast, the long-period commensurate structures such as 18O ($p = 4.500$), 14O ($p = 4.666$), 24O ($p = 4.800$), and 34O ($p = 4.857$) have not previously been investigated via *ab initio* methods.

Two kinds of commensurate $q = 2/5$ structures were considered in calculations, 10O and 10M. The 10O structure is orthorhombic, corresponding to Equation (1). 10O-like structures were

experimentally observed very close to the martensite transformation and were labeled as 10M^[13,37] (see also Figure 1).

The 10M commensurate structure has a five-layer modulation but is additionally monoclinic. It is typically observed at room temperature, near martensite transformation. Monoclinic distortion is not directly included in our anharmonic modulation model, as defined by Equation (1). If a model incorporating both precise modulation and the monoclinic distortion of the 10M structure is required, an approach treating these two phenomena independently can be considered.^[53] One might also regard the monoclinic distortion as an additional relaxation of the 10O structure, lowering the total energy by about 2 meV in uncorrected ($U = 0$) calculations. Notably, for $U = 0.5$ eV and larger, the structures and total energies of 10M and 10O martensites become nearly identical, i.e., the monoclinicity of 10M gets very small and thus irrelevant to our further discussion.

Having described the structures in Figure 8c, we now analyze how their energy profiles vary with U to determine their relative stability. For U in the range 0—1 eV, the 4O structure exhibits the lowest energy (highest stability). This does not correspond to the experiment since the 4O structure has never been observed in Ni-Mn-Ga. Nonetheless, $U = 0.5$ is sufficient to stabilize all structures with $p < 4.8$ ($q < 0.4167$) over the non-modulated martensite. With further increasing U , more structures with larger p become stabilized. At $U = 1.3$ eV, there is a shallow but definite minimum in the energy profile for the 14O structure at $p = 4.667$ ($q = 3/7$). For $U = 1.5$ eV and $U = 1.8$ eV, the minimum shifts to 34O structure at $p = 4.857$. Presumably, somewhere in the range $1.3 < U < 1.5$ eV, the energy minimum would also occur for the 24O structure, i.e., at $p = 4.800$. Thus, varying the Hubbard U parameter shifts the energy minimum, favoring LP-C states over the shortest-period commensurate (10M) and other structures such as 4O or NM.

However, the determined trends are primarily qualitative due to uncertain “right” localization correction parameter U and the narrow energy differences involved. The calculations were performed for Ni₅₀Mn₂₅Ga₂₅ rather than Ni₅₀Mn₂₈Ga₂₂, and the energy differences for $p > 4.5$ and $U > 1$ eV are on the edge of the method accuracy. Even for $U = 0$ eV, the computed energy values remain within a narrow 3.5 meV range. The key qualitative outcome is that, when electron localization correction is applied, the energy levels of the long-period and 10M commensurate states become nearly identical. Moreover, there appears to be a gradient—or even a shallow minimum—that favors one of the long-period structures (14O, 24O, or 34O). This is consistent with our experimental observations and the broader findings discussed in the following Section.

In summary, the DFT+ U calculations show that the lower energy of long-period commensurate states drives their stabilization over the short-period 10M commensurate structure. Additionally, our results reveal a significant sensitivity of the energy gradient with respect to p or q on the chosen Hubbard correction U . These findings further support the strong sensitivity of structural modulation on magnetic interactions, as previously reported.^[54]

2.6 Integrating the findings with literature data

In this Section, we compile the experimental and literature data on the modulation vector component q in the most relevant $\text{Ni}_{50}\text{Mn}_{25+x}\text{Ga}_{25-x}$ alloys and place them in the context of the newly identified long-period commensurate (LP-C) states. Then, we briefly discuss the causes of the modulation evolution.

Considering composition, alloys near the off-stoichiometric $\text{Ni}_{50}\text{Mn}_{28}\text{Ga}_{22}$, like the two studied here, are of particular practical interest because they exhibit the modulated martensite structure and resulting functionality at room temperature. Meanwhile, the stoichiometric $\text{Ni}_{50}\text{Mn}_{25}\text{Ga}_{25}$ (Ni_2MnGa), cubic at room temperature and transforming to martensite below ≈ 200 K, is also highly relevant as the archetypal Heusler alloy.

A graphical overview of the distribution of LP-C states along q is provided in **Figure 9a**. The compilation of our results and published data on q as a function of temperature is displayed in **Figure 9b**. These data exhibit composition- and temperature-dependent trends, with q converging to specific values (noting non-monotonous dependence of q on x): $3/7$ ($x \approx 0$), $5/12$ ($x \approx 3$), and $7/17$ ($x \approx 2$). These values represent the stable LP-C states: 14O, 24O, and 34O, respectively. The considerable scatter in the data likely reflects the wide range of sources and experimental conditions employed, such as different measurement techniques, sample preparation methods, sample histories, and the potential presence of twinning. It is also evident that single-temperature measurements are insufficient since only broader temperature ranges reveal convergence toward specific q values.

The $\text{Ni}_{50}\text{Mn}_{28}\text{Ga}_{22}$ alloy studied here, i.e., $x \approx 3$, undergoes martensite transformation slightly above room temperature. Near the transformation, at room temperature, the structure is typically commensurate or nearly commensurate ($q \approx 2/5$). Upon further cooling, the structure evolves toward 24O ($q = 5/12$). Measurements by Çakir et al.^[18] on an alloy with $x \approx 2$ shows q evolving toward 34O structure ($q = 7/17$).

The particular LP-C state occurring at low temperatures depends on composition. However, the noted non-monotonous dependence of low-temperature q on x suggests that it is also influenced by other factors such as chemical ordering, residual internal stress, or sample geometry. The model indicates that also other LP-C states (e.g., 38O, 58O) are possible, presumably arising for different compositions. For instance, one might speculate that $x \approx 1$ could lead to a low-temperature phase corresponding to 38O.

For stoichiometric alloys $\text{Ni}_{50}\text{Mn}_{25}\text{Ga}_{25}$ ($x = 0$), the measured q values cluster just below $3/7$, implying that this system prefers to transform into the 14O state. Except for one observation by Singh et al.^[33], no reports show $q > 3/7$. Moreover, the $q = 3/7$ (14O) in a Ni–Mn–Ga–Fe alloy marked the limit, beyond which the system transformed into the 14M martensite with seven-layer periodicity^[15].

The 14O structure with fourteen-layer periodicity can be described as a $(2\bar{3}2|\bar{2}3\bar{2})$ stacking sequence or as two nanotwin domains, each containing seven planes, **Figure 7d**. The 14M

structure, in contrast to 14O, is described as a $(\bar{2}5)_2$ stacking sequence, exhibiting a fourteen or seven-layer periodicity depending on whether chemical ordering is considered. Given the alignment between the periodicities of 14O (14 planes) and 14M (14 or 7 planes), it is unlikely that the system would stabilize in a phase beyond 14O with a periodicity below 14 layers, only to revert to 14-layer periodicity when transforming to 14M.

A theoretical approach based on generalized susceptibility links the modulation vector to Fermi-surface nesting, suggesting that an increase in the total magnetic moment per unit cell drives the transition from five-layer to seven-layer periodicity.^[55,56,54] This perspective is well complemented by the continuum-level approach^[57] in which a five-layer periodic displacement field becomes incommensurate when seven-layer periodicity emerges as an additional energy minimizer. The observed evolving incommensurate phase can thus be regarded as a *precursor to the eventual transition from a five-layer to a seven-layer periodicity*. Further, our empirical observation and theoretical reasoning indicate that $q = 3/7$, aligned to 7-layer periodicity, represents the upper limit for the five-layer modulated lattice. This is moreover supported by the fact that beyond 14O, there is only one additional LP-C state, 18O, with 9-layer periodicity. Thus, the 14O state marks the final stage of incommensurate precursor evolution before the emergence of 14M martensite. These findings motivate future investigations of the intermartensite transformation to the 14M phase, specifically the 14O→14M transition.

3 Conclusion and outlook

Our study establishes a comprehensive framework for understanding the thermal and compositional evolution of structural modulation in Ni-Mn-Ga alloys. By integrating diffraction experiments, theoretical modeling, and a stacking-sequence perspective, we found long-period commensurate (LP-C) states that unify two seemingly opposing concepts: wave modulation and a/b -nanotwinning. This duality emerges as the central result of this work, offering novel insights into the interplay between lattice distortions and microstructure. A thorough understanding and effective control of these modulation-induced microstructural features can significantly advance our ability to manipulate twin boundary mobility, thus enhancing material functionality.

The other key findings can be summarized as follows:

1. **Anharmonic incommensurate modulation:** Neutron and X-ray diffraction reveal that the martensite structures in the studied Ni-Mn-Ga alloys exhibit anharmonic incommensurate modulation. This leads to the appearance of high-order diffraction satellites, which are well captured by the proposed anharmonic modulation function, confirming the validity of our model.
2. **a/b -nanotwinning and structural symmetry:** The evolving incommensurate modulation drives the formation of periodic nanodomains identified as emerging a/b -nanotwins in the studied Ni-Mn-Ga alloy system. This structural evolution manifests as a transition from monoclinic to orthorhombic symmetry when nanodomain size gets below ≈ 20 nm.

3. **Long-period structures:** We enumerate a comprehensive set of LP-C structures with rational q values that are simultaneously a/b -nanotwins. These LP-C states provide a unifying link between continuous wave modulation and a/b -nanotwinning. Specific LP-C structures, namely 14O, 24O, and 34O, are detailed.
4. **Energy landscape and lock-in transition:** DFT+U calculations show that LP-C states can be energetically favored. Experiments and literature data identify the lock-in transitions to 14O, 24O, and 34O in $\text{Ni}_{50}\text{Mn}_{25}\text{Ga}_{25}$, $\text{Ni}_{50}\text{Mn}_{28}\text{Ga}_{25}$, and $\text{Ni}_{50}\text{Mn}_{27}\text{Ga}_{23}$, respectively.
5. **Modulation evolution:** Following the martensite transformation, the modulation is initially commensurate ($q = 2/5$) with five-layer periodicity. With further cooling, it becomes incommensurate due to the competition between the five-layer periodicity and the emerging seven-layer periodicity of the 14M phase. Along this evolution, the structure may lock into LP-C states (such as 14O, 24O, or 34O). We identify the 14O LP-C state ($q = 3/7$) as the final stage of the incommensurate precursor evolution before the 14M martensite emerges.

The insights gained from our microstructural interpretation of the evolving structure modulation not only elucidate the static structural features but also draw attention to related dynamic processes. In particular, *phasons*—low-energy collective excitations that adjust the phase of the modulation wave^[25]—could play a critical role in mediating structural and microstructural development. Shapiro et al.^[58] evidenced well-defined phasons in Ni–Mn–Ga, which was further supported by reports of anomalous diffuse scattering and superlattice peak broadening.^[33,59] Phasons may provide a mechanistic route for the transition through incommensurate structure and to long-period states. Specifically, a low-energy phasonic motion enabling local adjustments of the modulation wave phase can be crucial in nanodomain and a/b -nanotwin formation and annihilation, allowing the structure to rearrange toward lower-energy states.

From an elasticity and supermobility perspective, phasons could be essential in explaining the exceptionally soft shearing in Ni–Mn–Ga. Overall, phasons offer a mechanism to lower the elastic energy by facilitating local rearrangements of the modulation wave. While this perspective parallels an earlier study linking soft shearing to changes in the modulation stacking sequence^[6], the phason framework offers a more nuanced understanding of how soft shearing is enhanced. In contrast, the increasing density of $2\sqrt{2}$ faults with rising q seems to be the primary cause of soft shearing reduction, as the lattice softness and supermobility of five-layered martensite diminish upon approaching the 14M martensite.^[15,49]

Ultimately, integrating the phason framework with present findings on the links between structure modulation and larger structural features promises unprecedented control over the extraordinary elastic properties and supermobility of Ni–Mn–Ga. Future work on incorporating phason dynamics into predictive models of elastic behavior will pave the way for optimized functionality.

4 Experimental section

Sample preparation and measurement details

Single crystals of all studied alloys were grown at AdaptaMat Ltd. by a modified Bridgman method from high-purity raw components. The compositions were determined using X-ray fluorescence spectroscopy as $\text{Ni}_{50.0}\text{Mn}_{27.7}\text{Ga}_{22.3}$ and $\text{Ni}_{50.0}\text{Mn}_{28.1}\text{Ga}_{21.9}$ (at. %) for alloys 1 and 2, respectively. Samples, extracted from heat-treated ingots, were cut into rectangular parallelepipeds ($2.5 \times 3 \times 10 \text{ mm}^3$) with faces oriented approximately parallel to the $\{100\}$ planes of the parent cubic phase lattice. They were mechanically ground and subsequently electropolished as the final preparation step. The transformation temperatures were determined using DC magnetic susceptibility measurements: $M_s \approx M_f = 309 \text{ K}$, $A_s \approx A_f = 315 \text{ K}$ for alloy 1 and $M_s \approx M_f = 297 \text{ K}$, $A_s \approx A_f = 301 \text{ K}$ for alloy 2.

The five-layered martensite exhibits a deep four-level twinning hierarchy,^[2] which spans from macroscale to nanoscale. On macro- and mesoscale, the typically observed twins are so-called *a/c-twins* of Type 1 or Type 2 with $\{101\}$ or approximately $\{10\ 1\ 10\}$ twinning plane, respectively. The compound $\{100\}$ twins or *modulation twins* are typically seen on mesoscale as internal twins within *a/c-twins*. The modulation twins are further subdivided into *a/b-twins*, which typically form at scales of tens of micrometers or less. The *a/b-twins* are compound twins with a twinning plane of the $\{110\}$ type. They form due to a slight but non-negligible difference between the lattice parameters a and b . In the adaptive martensite concept^[11,41], the *a/b-twins* are internally twinned by the tetragonal adaptive nanotwins.

To ensure desired crystal orientations, all samples were mechanically compressed along the long geometrical axis before neutron diffraction (ND) and X-ray diffraction (XRD) experiments to create a nearly single-variant martensite state with the c -axis along the long geometrical axis. Initial orientation was achieved through diffraction setup adjustments, after which q -scans along the $[110]^*$ direction were performed. For ND, the scans included the $(2\bar{2}0)$ and (400) reflections and the enclosed satellites, and for XRD, the scans included the (400) and (620) reflections and respective satellites. Modulation was evaluated using both reciprocal space maps (XRD only) and q -scans (ND and XRD) at various temperatures.

The indexing of reflections followed previous studies by Fukuda et al.^[60], Mariager et al.^[61], and Righi et al.^[21], using the established wave modulation approach. The magnitude of the modulation vector component q was determined based on the relative positions of principal and satellite reflections. This approach ensures q is unaffected by thermal expansion because the modulation is confined to the $[110]^*$ direction. To account for minor instrumental factors like small sample displacements or orientation drifts during temperature changes, the satellite spacings were averaged to determine q .

Neutron diffraction experiments

The neutron diffraction (ND) experiments were conducted at ILL Grenoble using two four-circle neutron diffractometers equipped with He cryostats. The $\text{Ni}_{50}\text{Mn}_{27.7}\text{Ga}_{22.3}$ sample was measured using the D10 instrument employing a wavelength of $\lambda = 2.360 \text{ \AA}$,^[62] and the $\text{Ni}_{50}\text{Mn}_{28.1}\text{Ga}_{21.9}$ sample was measured using the D9 instrument with $\lambda = 0.838 \text{ \AA}$.^[63] Two-dimensional (2D) area detectors were utilized to accommodate small sample orientation changes during cooling or heating. In data analysis, the contributions from minor martensite variants and background noise were minimized by restricting the 2D integration area. A detailed description of the data processing methodology is available in the Supplementary Material of a related publication.^[22]

X-Ray diffraction experiments

The X-ray diffraction (XRD) measurements were performed using a Bruker D8 Discover diffractometer with a rotating Cu anode ($\lambda = 0.1542 \text{ nm}$) equipped with Anton Paar DCS 350 cooling stage and a point detector. The samples were precompressed to achieve a nearly single martensite variant state, orienting the *c*-axis uniformly across the sample. Reciprocal space mapping was conducted to confirm that the modulation direction was consistent, and scans included reflections such as (400) and (620) with their associated modulation satellites.

Model calculations of diffraction patterns

The DISCUS simulation package^[64] was employed to model diffraction patterns. Simulations were performed by averaging data from 20 crystal models, each consisting of $470 \times 2 \times 1$ unit cells. The base unit cell was $4.21 \times 4.22 \times 5.65 \text{ \AA}$, corresponding to a composition of $\text{Ni}_{50}\text{Mn}_{25}\text{Ga}_{25}$. Tests increasing Mn content to $\text{Ni}_{50}\text{Mn}_{28}\text{Ga}_{22}$ revealed no significant impact on the calculated diffraction patterns along $[110]^*$.

Details of ab initio calculations

The ab initio calculations based on DFT+U were performed for $\text{Ni}_{50}\text{Mn}_{25}\text{Ga}_{25}$ composition. This is slightly different from the experimental composition of $\text{Ni}_{50}\text{Mn}_{28}\text{Ga}_{22}$ and presumably causes only small differences between computational and experimental results. These differences are acknowledged but omitted from further discussion to maintain clarity.

DFT+U calculations were performed using the Vienna Ab initio Simulation Package (VASP)^[65,66] with projector-augmented wave (PAW) potentials.^[67,68] The electronic orbitals were expanded using plane waves with a maximum kinetic energy of 800 eV, explicitly including the $3p^6 3d^9 4s^1$ electrons for Ni, $3p^6 3d^6 4s^1$ for Mn, and $3d^{10} 4s^2 4p^1$ for Ga as valence states. The Brillouin zone was sampled using a Γ -point-centered mesh with a minimum k-point spacing of 0.08 \AA^{-1} . The Methfessel-Paxton smearing method^[69] (smearing width parameter: 0.07 eV) was used for initial relaxations, followed by recalculations of total energies using the modified tetrahedron method^[70] to ensure precision. The gradient-corrected exchange-correlation functional (GGA) proposed by Perdew, Burke, and Ernzerhof was employed, including non-spherical contributions inside the PAW spheres. The rotationally invariant DFT+U method proposed by Dudarev^[71] was applied to address electron localization.

Previous studies showed that DFT results deviated significantly from experiments without electron-localization correction (U). Most notably, the calculated 10M structure exhibited overestimated monoclinicity and significantly different a and b axes (5% difference in uncorrected calculation vs $\approx 0.5\%$ in the experiment)^[42]. Furthermore, a 4O structure emerged as the most stable despite never being experimentally observed in Ni–Mn–Ga^[39]. This highlights a known limitation of standard DFT (U=0) for Ni–Mn–Ga.

A range of U values from 0.50 eV to 5.97 eV for Mn atoms has been proposed. However, large U hinders the martensitic transformation as the cubic parent phase of austenite becomes the most stable structure^[72]. The best agreement between calculated and experimental lattice parameters was reached for U = 1.8 eV^[42], whereas Bhattacharya et al.^[73] found that U = 0.5 eV provides the best agreement between calculated and experimentally measured hard x-ray photoelectron spectra of 14M martensite. Therefore, we calculated the energy landscape for U from 0 to 1.8 eV. Note that selecting the exact U value was not the goal of this work.

Input computational cells with orthorhombic lattices for modulated martensites were generated using the anharmonic modulation function described in Equation (1). Full relaxation of atomic positions and structural parameters was carried out using the quasi-Newton algorithm, with convergence criteria set to < 0.01 meV/atom. To minimize errors due to cell size differences, energies of modulated structures were always calculated relative to those of non-modulated martensite in cells with identical numbers of atoms. Convergence tests confirmed that this setup provided total energy estimates with an accuracy better than 0.1 meV/atom.

Acknowledgment

P.V. and L.S. contributed equally to this work. The authors acknowledge the Institut Laue-Langevin (ILL) for the beam time allocated^[62,63], the funding support from the Czech Science Foundation [grant number 24-10334], Brno University of Technology [project number FSI-S-20-6313], and the assistance provided by the Ferroic Multifunctionalities project, supported by the Ministry of Education, Youth, and Sports of the Czech Republic [Project No. CZ.02.01.01/00/22_008/0004591], co-funded by the European Union. Computational resources were provided by the Ministry of Education, Youth and Sports of the Czech Republic under the Projects e-INFRA CZ (ID:90140) at the IT4Innovations National Supercomputing Center. We thank L. Klimša for assistance with scanning electron microscopy measurements.

References

- [1] M. Acet, Ll. Mañosa, A. Planes, In *Handbook of Magnetic Materials* (Ed.: Buschow, K. H. J.), Elsevier, **2011**, pp. 231–289.
- [2] L. Straka, O. Heczko, H. Seiner, N. Lanska, J. Drahokoupil, A. Soroka, S. Fähler, H. Hänninen, A. Sozinov, *Acta Materialia* **2011**, *59*, 7450.
- [3] I. Aaltio, A. Sozinov, Y. Ge, K. Ullakko, V. K. Lindroos, S.-P. Hannula, *Giant Magnetostrictive Materials*, Elsevier BV, **2016**.
- [4] D. Shilo, E. Faran, B. Karki, P. Müllner, *Acta Materialia* **2021**, *220*, 117316.
- [5] O. Heczko, H. Seiner, S. Fähler, *MRS Bulletin* **2022**, *47*, 618.
- [6] K. Repček, P. Stoklasová, T. Grabec, P. Sedlák, J. Olejňák, M. Vinogradova, A. Sozinov, P. Veřtát, L. Straka, O. Heczko, H. Seiner, *Advanced Materials* **2024**, *36*, 2406672.
- [7] O. Heczko, N. Scheerbaum, O. Gutfleisch, In *Nanoscale Magnetic Materials and Applications* (Eds.: Liu, J. P.; Fullerton, E.; Gutfleisch, O.; Sellmyer, D. J.), Springer US, Boston, MA, **2009**, pp. 399–439.
- [8] A. Saren, A. R. Smith, K. Ullakko, *Microfluid Nanofluid* **2018**, *22*, 38.
- [9] X. Zhang, M. Qian, In *Magnetic Shape Memory Alloys: Preparation, Martensitic Transformation and Properties* (Eds.: Zhang, X.; Qian, M.), Springer, Singapore, **2022**, pp. 255–268.
- [10] Z. A. D. Lethbridge, R. I. Walton, A. S. H. Marmier, C. W. Smith, K. E. Evans, *Acta Materialia* **2010**, *58*, 6444.
- [11] S. Kaufmann, R. Niemann, T. Thersleff, U. K. Rößler, O. Heczko, J. Buschbeck, B. Holzapfel, L. Schultz, S. Fähler, *New Journal of Physics* **2011**, *13*, 053029.
- [12] M. Vronka, L. Straka, M. Klementová, L. Palatinus, P. Veřtát, A. Sozinov, O. Heczko, *Scripta Materialia* **2024**, *242*, 115901.
- [13] R. Chulist, A. Wójcik, A. Sozinov, T. Tokarski, M. Faryna, N. Schell, W. Skrotzki, B. Li, H. Sehitoglu, X. Li, W. Maziarz, *Advanced Functional Materials* **2024**, *34*, 2307322.
- [14] L. Righi, F. Albertini, L. Paretì, A. Paoluzi, G. Calestani, *Acta Materialia* **2007**, *55*, 5237.
- [15] P. Veřtát, H. Seiner, L. Straka, M. Klicpera, A. Sozinov, O. Fabelo, O. Heczko, *J. Phys.: Condens. Matter* **2021**, *33*, 265404.
- [16] Y. Ge, L. Straka, M. Vronka, M. Rameš, A. Sozinov, O. Heczko, *Materials Characterization* **2022**, *190*, 112007.
- [17] L. Righi, F. Albertini, A. Paoluzi, S. Fabbrici, E. Villa, G. Calestani, S. Besseghini, In *Materials Science Forum*, Trans Tech Publ, **2010**, pp. 33–41.
- [18] A. Çakır, M. Acet, L. Righi, F. Albertini, M. Farle, *AIP Advances* **2015**, *5*, 097222.
- [19] A. Pramanick, X. P. Wang, K. An, A. D. Stoica, J. Yi, Z. Gai, C. Hoffmann, X.-L. Wang, *Phys. Rev. B* **2012**, *85*, 144412.
- [20] Y. Zhou, J. Long, J. Fan, S. Ouyang, N. Jin, *Materials Characterization* **2024**, *208*, 113612.
- [21] L. Righi, *Metals* **2021**, *11*, 1749.
- [22] P. Veřtát, M. Klicpera, O. Fabelo, O. Heczko, L. Straka, *Scripta Materialia* **2024**, *252*, 116251.
- [23] V. Martynov, V. Kokorin, *Journal de Physique III* **1992**, *2*, 739.
- [24] O. Heczko, P. Cejpek, J. Drahokoupil, V. Holý, *Acta Materialia* **2016**, *115*, 250.
- [25] P. Bak, *Rep. Prog. Phys.* **1982**, *45*, 587.
- [26] P. Bak, *Physics Today* **1986**, *39*, 38.
- [27] Y. Yamada, N. Hamaya, *Journal of the Physical Society of Japan* **1983**, *52*, 3466.

- [28] P. Bak, J. von Boehm, *Phys. Rev. B* **1980**, 21, 5297.
- [29] L. Straka, J. Drahokoupil, P. Veřtát, M. Zelený, J. Kopeček, A. Sozinov, O. Heczko, *Scientific reports* **2018**, 8, 1.
- [30] J. M. Pérez-Mato, G. Madariaga, *Solid State Communications* **1986**, 58, 105.
- [31] L. Palatinus, S. van Smaalen, *Zeitschrift für Kristallographie - Crystalline Materials* **2004**, 219, 719.
- [32] J. C. Marmeggi, G. H. Lander, S. van Smaalen, T. Brückel, C. M. E. Zeyen, *Phys. Rev. B* **1990**, 42, 9365.
- [33] S. Singh, V. Petricek, P. Rajput, A. H. Hill, E. Suard, S. R. Barman, D. Pandey, *Physical Review B* **2014**, 90, 014109.
- [34] X. Balandraud, G. Zanzotto, *Journal of the Mechanics and Physics of Solids* **2007**, 55, 194.
- [35] V. Jusuf, R. S. Elliott, *Journal of the Mechanics and Physics of Solids* **2020**, 138, 103879.
- [36] M. Vinogradova, A. Sozinov, L. Straka, P. Veřtát, O. Heczko, M. Zelený, R. Chulist, E. Lähderanta, K. Ullakko, *Acta Materialia* **2023**, 255, 119042.
- [37] L. Straka, J. Drahokoupil, P. Veřtát, J. Kopeček, M. Zelený, H. Seiner, O. Heczko, *Acta Materialia* **2017**, 132, 335.
- [38] M. E. Gruner, R. Niemann, P. Entel, R. Pentcheva, U. K. Rößler, K. Nielsch, S. Fähler, *Scientific reports* **2018**, 8, 1.
- [39] M. Zelený, L. Straka, A. Sozinov, O. Heczko, *Phys. Rev. B* **2016**, 94, 224108.
- [40] A. G. Khachatryan, S. M. Shapiro, S. Semenovskaya, *Physical Review B* **1991**, 43, 10832.
- [41] R. Niemann, U. K. Rößler, M. E. Gruner, O. Heczko, L. Schultz, S. Fähler, *Advanced Engineering Materials* **2012**, 14, 562.
- [42] M. Zelený, P. Sedlák, O. Heczko, H. Seiner, P. Veřtát, M. Obata, T. Kotani, T. Oda, L. Straka, *Materials & Design* **2021**, 209, 109917.
- [43] R. Chulist, L. Straka, N. Lanska, A. Soroka, A. Sozinov, W. Skrotzki, *Acta Materialia* **2013**, 61, 1913.
- [44] O. Heczko, L. Klimša, J. Kopeček, *Scripta Materialia* **2017**, 131, 76.
- [45] H. Seiner, R. Chulist, W. Maziarz, A. Sozinov, O. Heczko, L. Straka, *Scripta Materialia* **2019**, 162, 497.
- [46] A. Saren, A. Sozinov, S. Kustov, K. Ullakko, *Scripta Materialia* **2020**, 175, 11.
- [47] Y. U. Wang, *Physical Review B* **2006**, 74, 104109.
- [48] Y. U. Wang, *Phys. Rev. B* **2007**, 76, 024108.
- [49] L. Straka, A. Sozinov, J. Drahokoupil, V. Kopecký, H. Hänninen, O. Heczko, *Journal of Applied Physics* **2013**, 114, 063504.
- [50] M. Vinogradova, A. Sozinov, L. Straka, P. Veřtát, O. Heczko, M. Zelený, R. Chulist, K. Ullakko, *Scripta Materialia* **2024**, 247, 116096.
- [51] P. Cejpek, D. Drozdenko, K. Mathis, R. H. Colman, M. Dopita, L. Straka, O. Heczko, *Acta Materialia* **2023**, 257, 119133.
- [52] H. Seiner, M. Zelený, P. Sedlák, L. Straka, O. Heczko, *physica status solidi (RRL) – Rapid Research Letters* **2022**, 16, 2100632.
- [53] J. B. Lu, H. X. Yang, H. F. Tian, L. J. Zeng, C. Ma, L. Feng, G. H. Wu, J. Q. Li, J. Jansen, *Journal of Solid State Chemistry* **2010**, 183, 425.
- [54] J. Luštinec, M. Obata, R. Majumder, K. Hyodo, T. Kotani, L. Kalvoda, T. Oda, *Journal of the Magnetism Society of Japan* **2024**, 48, 94.
- [55] O. I. Velikokhatnyi, I. I. Naumov, *Phys. Solid State* **1999**, 41, 617.
- [56] M. Obata, T. Kotani, T. Oda, *Phys. Rev. Mater.* **2023**, 7, 024413.
- [57] B. Benešová, M. Frost, M. Kampschulte, C. Melcher, P. Sedlák, H. Seiner, *Phys. Rev. B* **2015**, 92, 180101.
- [58] S. M. Shapiro, P. Vorderwisch, K. Habicht, K. Hradil, H. Schneider, *EPL* **2007**, 77, 56004.

- [59] R. I. Barabash, O. M. Barabash, E. A. Karapetrova, M. E. Manley, *Applied Physics Letters* **2014**, *104*, 241905.
- [60] T. Fukuda, H. Kushida, M. Todai, T. Kakeshita, H. Mori, *Scripta Materialia* **2009**, *61*, 473.
- [61] S. O. Mariager, T. Huber, G. Ingold, *Acta materialia* **2014**, *66*, 192.
- [62] M. Klicpera, O. R. Fabelo Rosa, O. Heczko, L. Straka, P. Veřtát, *Investigation of commensurate-incommensurate structure modulation transitions in Ni-Mn-Ga-Fe martensite*, <https://doi.ill.fr/10.5291/ILL-DATA.5-15-626>, **2019**.
- [63] M. Klicpera, O. R. Fabelo Rosa, O. Heczko, L. Straka, P. Veřtát, *Intermartensitic transformations and search for the ground state in Ni-Mn-Ga single crystals exhibiting the magnetic shape memory effect*, <https://doi.ill.fr/10.5291/ILL-DATA.5-41-950>, **2018**.
- [64] T. Proffen, R. B. Neder, *J Appl Cryst* **1997**, *30*, 171.
- [65] G. Kresse, J. Furthmüller, *Phys. Rev. B* **1996**, *54*, 11169.
- [66] G. Kresse, J. Furthmüller, *Computational Materials Science* **1996**, *6*, 15.
- [67] P. E. Blöchl, *Phys. Rev. B* **1994**, *50*, 17953.
- [68] G. Kresse, D. Joubert, *Phys. Rev. B* **1999**, *59*, 1758.
- [69] M. Methfessel, A. T. Paxton, *Phys. Rev. B* **1989**, *40*, 3616.
- [70] P. E. Blöchl, O. Jepsen, O. K. Andersen, *Phys. Rev. B* **1994**, *49*, 16223.
- [71] S. L. Dudarev, G. A. Botton, S. Y. Savrasov, C. J. Humphreys, A. P. Sutton, *Phys. Rev. B* **1998**, *57*, 1505.
- [72] B. Himmetoglu, V. M. Katukuri, M. Cococcioni, *J. Phys.: Condens. Matter* **2012**, *24*, 185501.
- [73] J. Bhattacharya, P. Sadhukhan, S. Sarkar, V. K. Singh, A. Gloskovskii, S. R. Barman, A. Chakrabarti, *Phys. Rev. B* **2023**, *108*, L121114.
- [74] J. Pons, V. A. Chernenko, R. Santamarta, E. Cesari, *Acta Materialia* **2000**, *48*, 3027.
- [75] Y. Ge, H. Jiang, A. Sozinov, O. Söderberg, N. Lanska, J. Keränen, E. I. Kauppinen, V. K. Lindroos, S.-P. Hannula, *Materials Science and Engineering: A* **2006**, *438–440*, 961.
- [76] H. Kushida, K. Fukuda, T. Terai, T. Fukuda, T. Kakeshita, T. Ohba, T. Osakabe, K. Kakurai, K. Kato, *Eur. Phys. J. Spec. Top.* **2008**, *158*, 87.
- [77] H. Kushida, K. Fukuda, T. Terai, T. Fukuda, T. Kakeshita, T. Ohba, T. Osakabe, K. Kakurai, K. Kato, *J. Phys.: Conf. Ser.* **2009**, *165*, 012054.

Figure 1. **a)** Schematic phase diagram of $\text{Ni}_{50}\text{Mn}_{25+x}\text{Ga}_{25-x}$ system^[29] with the measurement paths marked. **b)** Representative neutron diffraction for alloy 2 (300 K \rightarrow 2 K), showing q evolution and the emergence of unusual high-order satellites in the incommensurate structure, marked by red arrows. **c)** The evolution of q with temperature for $x = 2.7$, i.e., alloy 1, $\text{Ni}_{50.0}\text{Mn}_{27.7}\text{Ga}_{22.3}$. The inset shows modulation direction and cubic and diagonal coordinates ($c \equiv b_d$ are oriented out of the paper plane). **d)** The evolution of q with temperature for $x = 3.1$, i.e., alloy 2, $\text{Ni}_{50.0}\text{Mn}_{28.1}\text{Ga}_{21.9}$. *References to individual regions in (a):* a very narrow region of 10M' near the martensite transformation^[13,37], five-layered modulated 10M martensite with $a > b$ ^[23,74,75], nanotwinned martensite with $a = b$ ^[29], 14M, NM martensite—seven-layered modulated and tetragonal non-modulated martensites,^[16,23,74] Saren2020—alloy where coarse a/b -twins were observed optically by Saren et al.^[46]

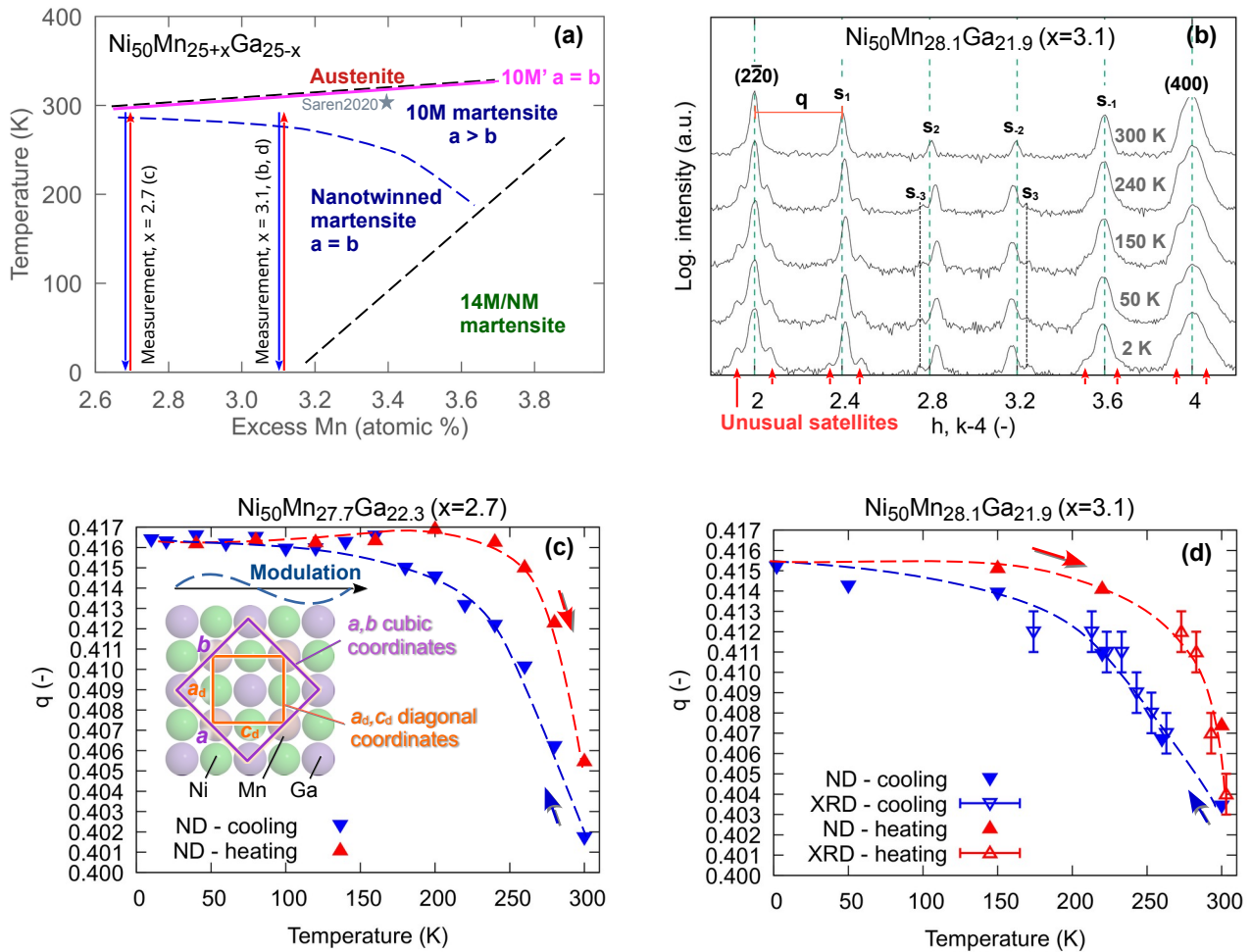


Figure 2. Selected experimental X-ray diffraction patterns showing the evolution of q upon cooling in alloy 2, $\text{Ni}_{50.0}\text{Mn}_{28.1}\text{Ga}_{21.9}$, compared with the model diffraction patterns calculated using the modulation function from Equation (1), at temperatures: **a)** 263 K, **b)** 233 K, **c)** 223 K, **d)** 174 K. High-order satellites from the $(2\bar{2}0)$ reflection are marked in (d).

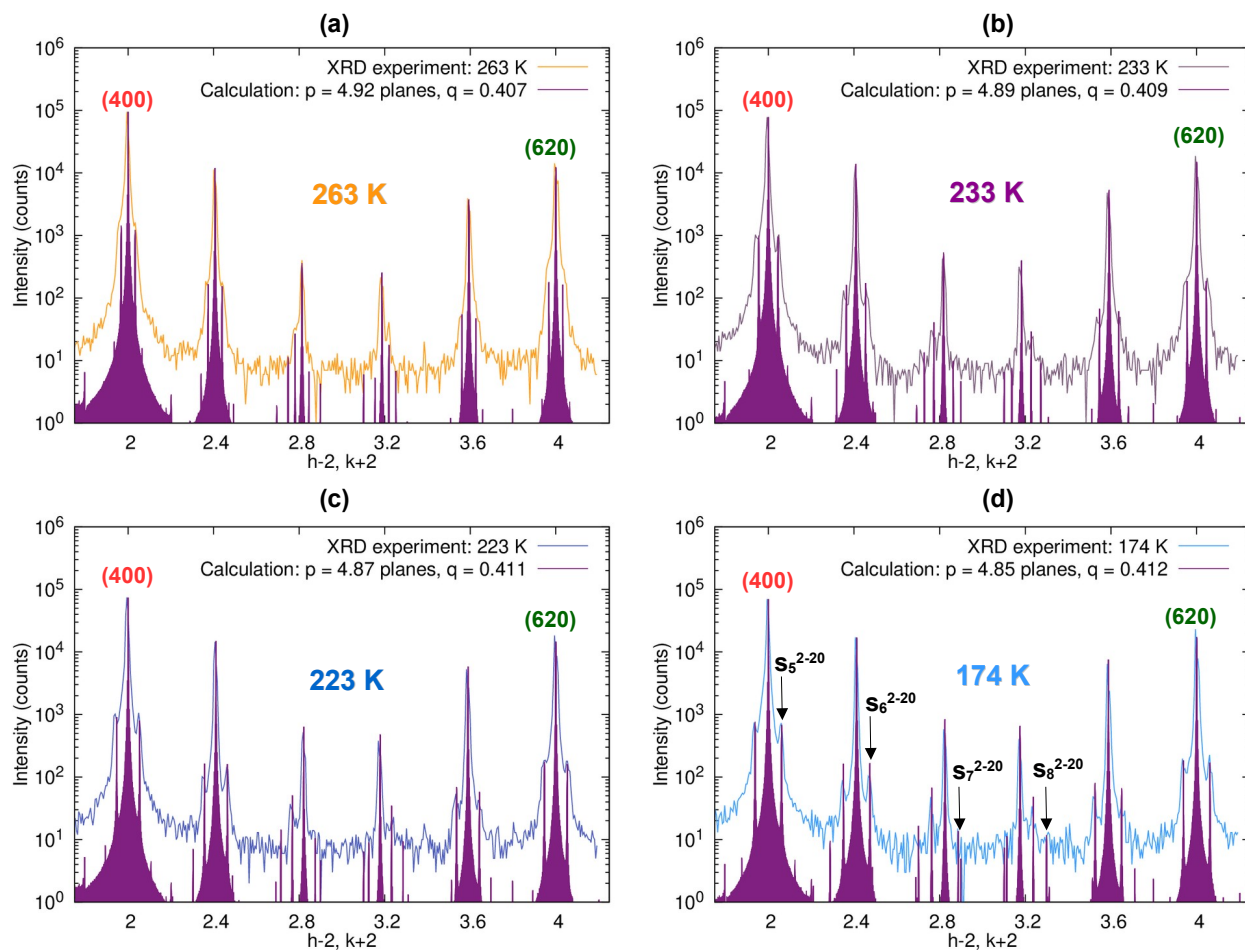


Figure 3. Anharmonic structure modulation with $q = 2/5$, with the interpretation of the displacements as a $(2\bar{3})_2$ stacking sequence illustrated: **a)** Scaled to the lattice. **b)** Displacements threefold exaggerated for clearer visibility of the stacking sequence. **c)** Modulation function (red curve) juxtaposed with lattice periodicity (vertical lines), determining plane displacements.

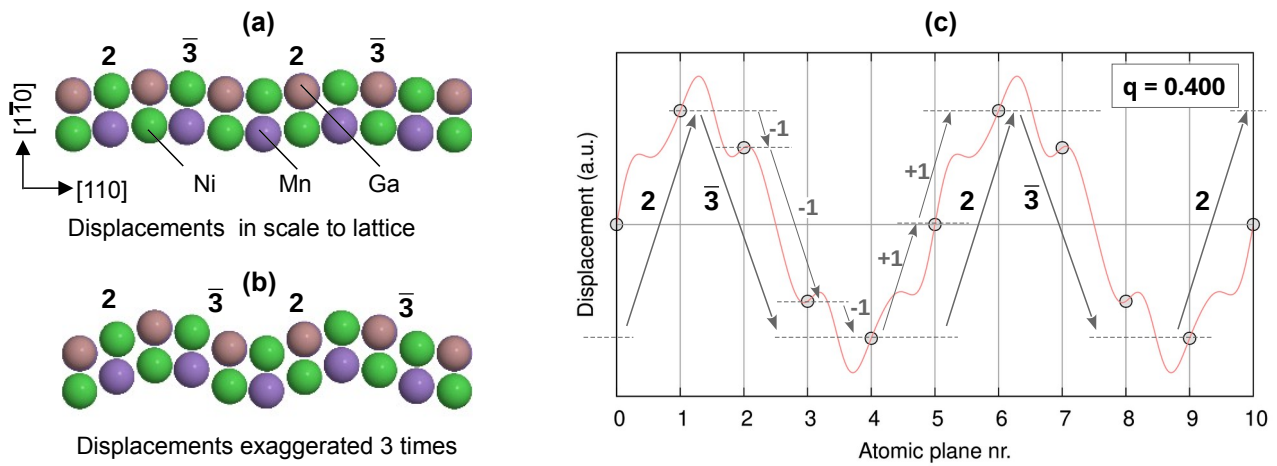


Figure 4. Insights into nanodomain (*a/b*-nanotwin) formation arising from the slightly different periodicity of modulation and lattice: **a)** General principle of wave mixing known, e.g., from acoustics – adding two harmonic signals of different frequency results in “beats” with frequency $|f_1 - f_2|$. **b)** General principle corresponding to the studied case: interaction of a continuous harmonic wave (modulation function) with a train of narrow pulses (lattice) also results in “beats” or a periodic “envelope.” **c)** Application to the studied compound: comparison of commensurate modulation ($q = 0.400$) with displacements aligned uniformly with the lattice and incommensurate modulation ($q = 0.412$), where the different periodicity of the lattice and modulation leads to plane displacements following the “envelope”. Interpreting the displacements as a stacking sequence reveals reversals between $\bar{3}2$ and $\bar{2}3$ stackings, marking the formation of nanodomains identified as *a/b*-nanotwins. The vertical green line marks $2\sqrt{2}$ nanotwin boundary. **d)** A larger-scale depiction for $q = 0.400, 0.406, 0.412$, revealing different envelope periods, i.e., (nano)domain sizes (green dimension lines), and $\bar{2}\sqrt{2}$ and $2\sqrt{2}$ nanotwin boundaries (vertical green lines).

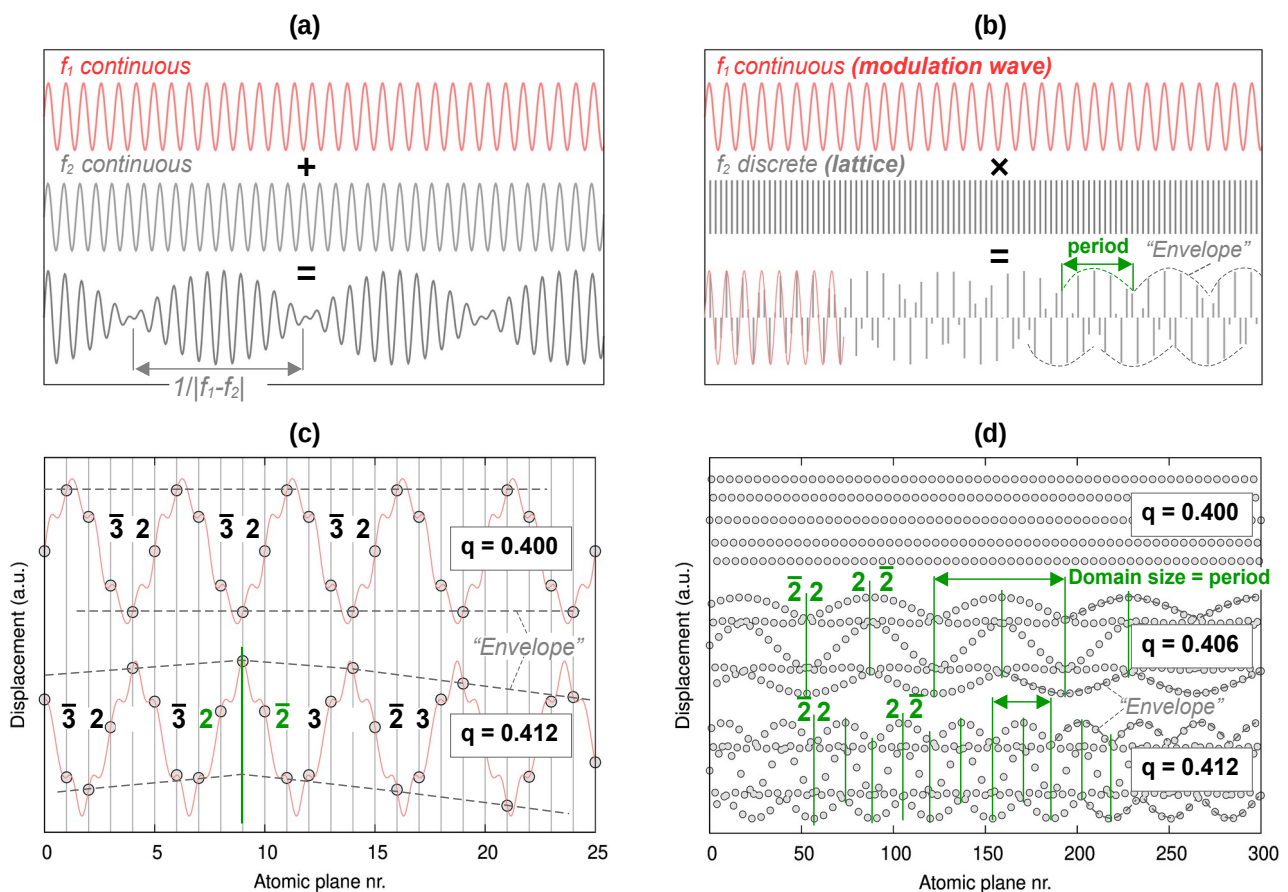


Figure 5. Evolution of the size of a/b twin bands with cooling as observed in an experiment using scanning electron microscope and BSE contrast in alloy $\text{Ni}_{50.0}\text{Mn}_{28.2}\text{Ga}_{21.8}$ ($x=3.2$). The contrast in the boxed regions has been adjusted post-acquisition to improve visibility. The nearly vertical interface is an a/c twin boundary. **a)** At 298 K, $q \approx 0.400$, broad twin bands oriented horizontally are discernible, some indicated by white arrows. **b)** At 253 K, $q > 0.400$, significantly finer twin bands emerge in the same region.

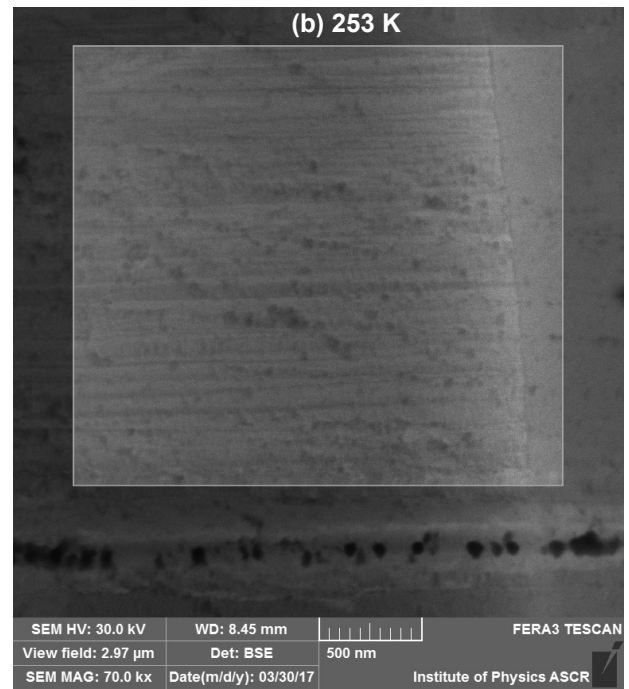
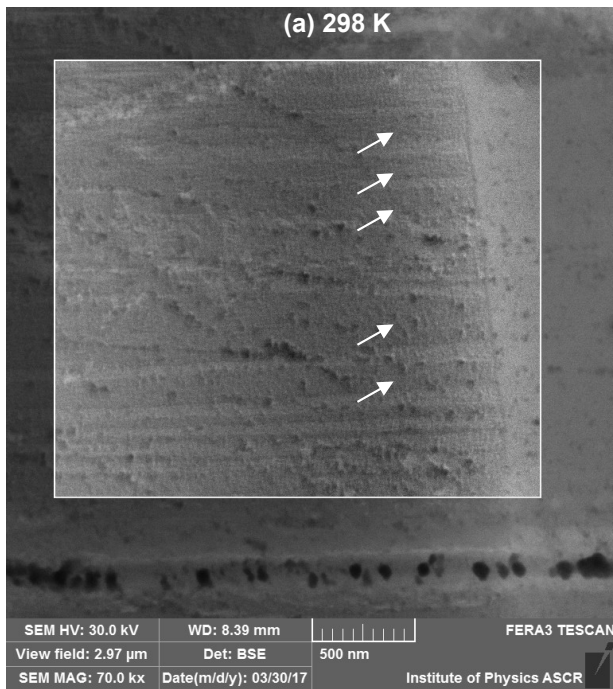


Figure 6. **a)** Relationship between temperature and domain (a/b twin) size, derived from Equation (3) using the measured $q(T)$ dependence in alloy 1, $\text{Ni}_{50.0}\text{Mn}_{27.7}\text{Ga}_{22.3}$. Lattice parameters a , b (up-triangles and down-triangles, respectively) are charted, and the intervals of monoclinic and orthorhombic symmetry are marked (red and blue colors/regions, respectively) as defined by the adaptive diffraction condition (domain size $DS < \approx 20$ nm, horizontal dashed line). The relation between a , b lattice parameters and symmetry is illustrated in the inset. **b)** Representation of long-period state formation using $p = 5 - 1/N$, Equation (4), with $N = 3$ as an example. **c)** Relationship between domain size and q determined using Equation (3) with marked near-room temperature monoclinic structures: 10M commensurate (10M (C)), 10M incommensurate (10M (IC)), and specific low-temperature orthorhombic structures 34O, 24O, and 14O. The dashed magenta line and right axis show the density of $2|\bar{2}$ interfaces (a/b -nanotwin boundaries). **d)** Tensile-deformation experiment: q is measured at room temperature as a function of tensile strain along the $[100]$ direction (a -axis).

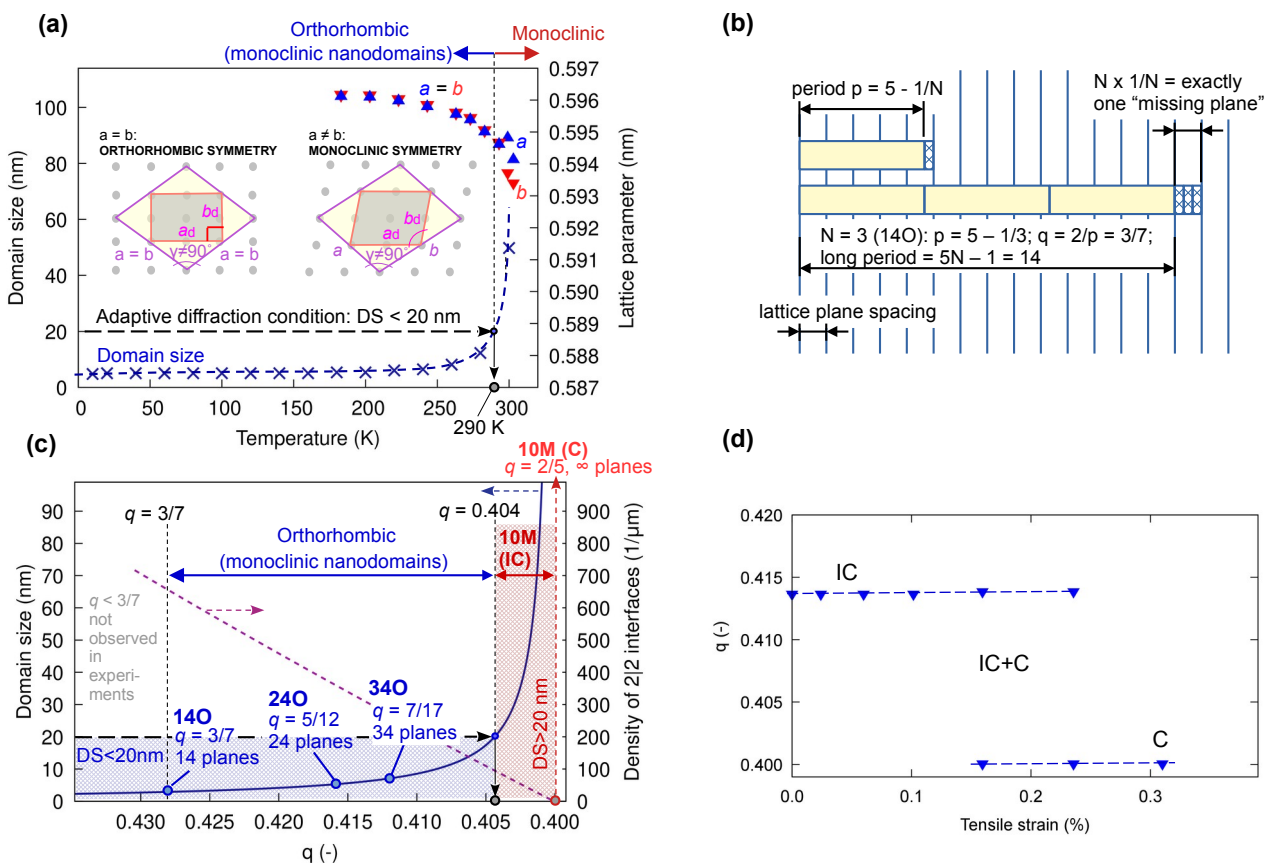


Figure 8. **a)** Comparison between the harmonic modulation (dashed line), the determined anharmonic modulation function (solid red line), Equation (1), and the DFT-calculated displacements (filled symbols) in the 24O structure for Hubbard correction parameter $U = 0, 0.5, 1.3,$ and 1.8 eV. Relative displacements exhibit nearly identical waveforms for all U , but maximum displacements (amplitudes) vary slightly, as shown in (b). **b)** Maximum modulation displacements as a function of U and the corresponding experimental maximum modulation displacements determined from ND data for alloy 1 and 2. **c)** Total energy landscape, relative to the non-modulated martensite, as a function of $p = 2/q$ and U . Individual structures corresponding to a specific modulation period p are marked. The inset illustrates the difference between the 10O and 10M structures: both have similar five-layer modulation but differ in unit cell symmetry (orthorhombic vs monoclinic).

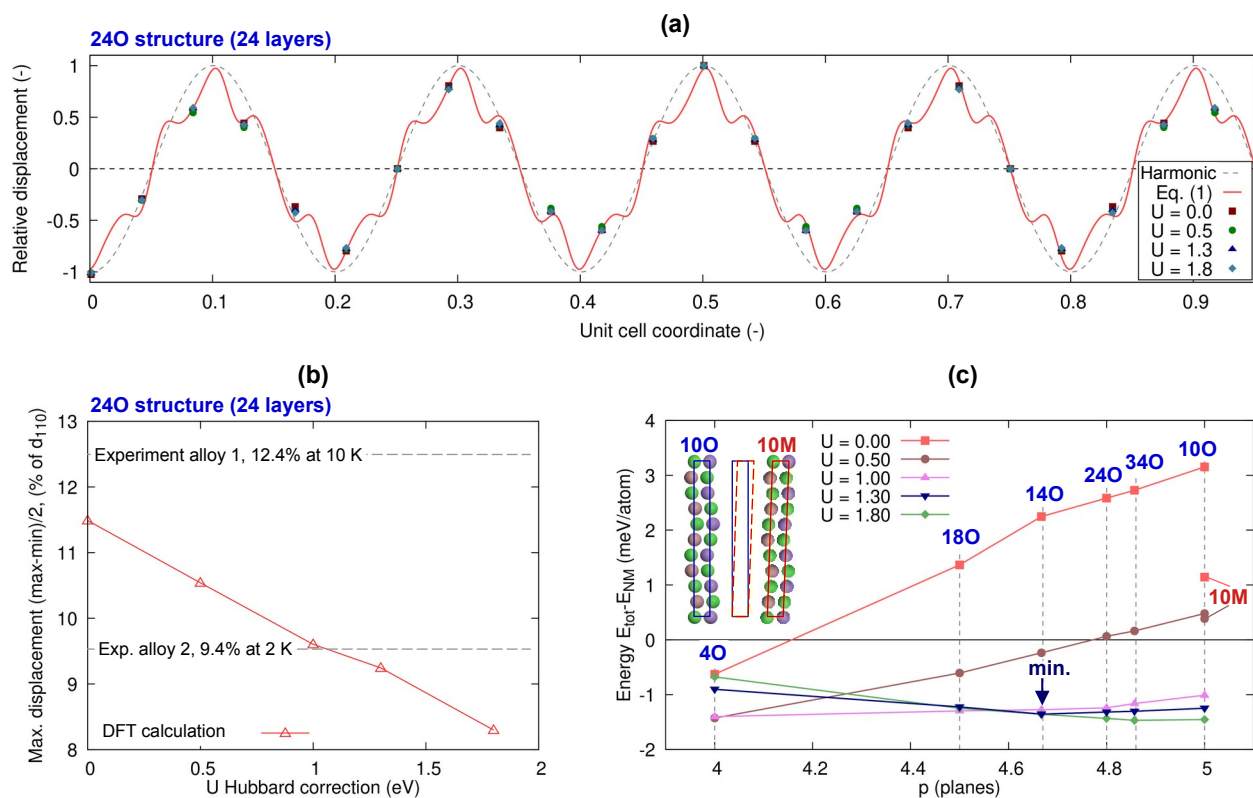


Figure 9. a) Distribution of the 10M commensurate, 10M incommensurate, and long-period commensurate states along q (vertically). b) Modulation vector component q as a function of temperature. Dashed curves and lines are only guides for the eye. The evolution of $q(T)$, converging towards the 140, 240, and 340 states, indicates that these (a/b -nanotwinned) long-period commensurate states are stable at low temperatures. Data were compiled from this study and previous literature (see legend): Righi 2007^[14], Fukuda 2009^[60], Kushida 2008^[76], Kushida 2009^[77], Righi 2010^[17], Mariager 2014^[61], Singh 2014^[33], Çakir 2015^[18], Righi 2021.^[21]

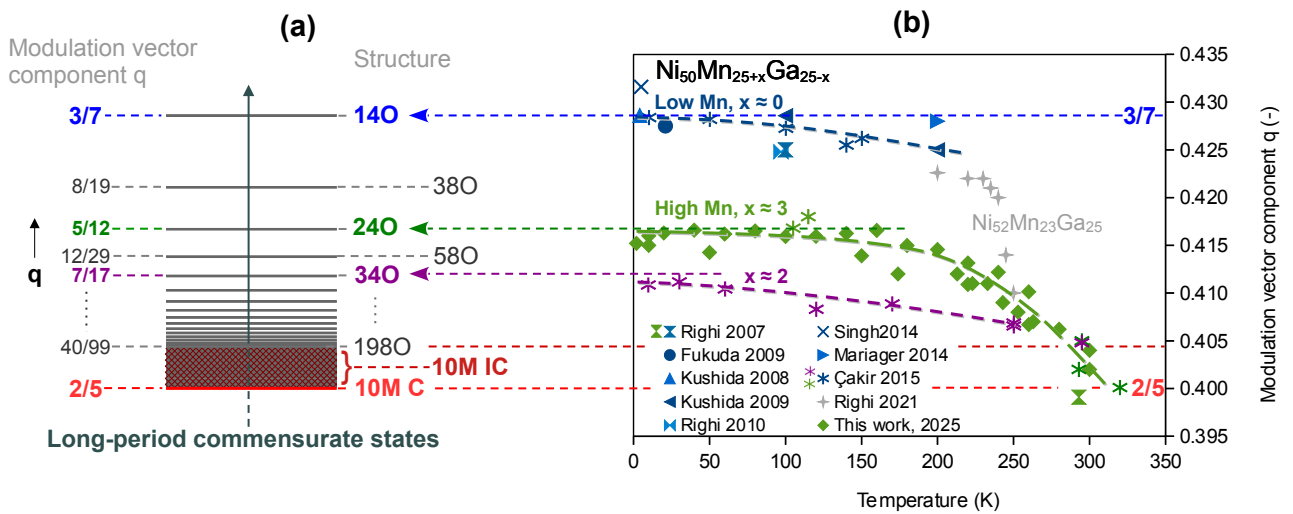


Table 1. Long-period commensurate structures derived using Equations (3)–(5).

N	period p (planes)	q = 2/p (-)	q as a ratio (-)	Domain size (planes)	Domain size (nm)	Marking	Alternative marking	Observed in experiment
1	4.000	0.5000	1/2 (=2/4)	4	0.8	4O*	4.000O	no*
2	4.500	0.4444	4/9	9	1.9	18O#	4.500O	no
3	4.667	0.4286	3/7 (=6/14)	14	2.9	14O	4.667O	yes
4	4.750	0.4211	8/19	19	4.0	38O#	4.750O	:
5	4.800	0.4167	5/12 (=10/24)	24	5.0	24O	4.800O	yes
6	4.833	0.4138	12/29	29	6.1	58O#	4.833O	:
7	4.857	0.4118	7/17 (=14/34)	34	7.1	34O	4.857O	yes
8	4.875	0.4103	16/39	39	8.2	78O#	:	:
9	4.889	0.4091	9/22 (=18/44)	44	9.2	44O	4.889O	:
10	4.900	0.4082	20/49	49	10.3	98O#	4.900O	:
11	4.909	0.4074	11/27 (=22/54)	54	11.3	54O	:	:
12	4.917	0.4068	24/59	59	12.4	118O#	:	:
:	:	:	:	:	:	:	:	:
> 20	> 4.95	< 0.404	< 40/99	> 99	> 20	10M (IC)*	> 4.950M or 5M (IC)	yes :
:	:	:	:	:	:	:	:	:
∞	5.000	0.400	2/5	∞	∞	10M (C)*	5M (C)	yes

* Theoretically predicted but not observed in experiment.

Double cell size to comply with the L₂ order. Ordering ignored for domain size determination.

x Often marked also as 5M when neglecting ordering (C = commensurate, IC = incommensurate); see also discussion on 10O in text.